Journal of Hydrometeorology

Increasing the depth of a Land Surface Model. Part II: Temperature sensitivity to improved subsurface thermodynamics and associated permafrost response

--Manuscript Draft--

Manuscript Number:	JHM-D-21-0023
Full Title:	Increasing the depth of a Land Surface Model. Part II: Temperature sensitivity to improved subsurface thermodynamics and associated permafrost response
Article Type:	Article
Corresponding Author:	Norman Julius Steinert Universidad Complutense de Madrid Madrid, SPAIN
Corresponding Author's Institution:	Universidad Complutense de Madrid
First Author:	Norman Julius Steinert
Order of Authors:	Norman Julius Steinert
	Jesus Fidel González-Rouco
	Philipp de Vrese
	Elena García-Bustamante
	Stefan Hagemann
	Camilo Melo-Aguilar
	Johann H. Jungclaus
	Stephan J. Lorenz
Abstract:	The impact of various modifications of the JSBACH Land Surface Model to represent soil temperature and cold-region hydro-thermodynamic processes in climate projections of the 21st century is examined. We explore the sensitivity of JSBACH to changes in the soil thermodynamics, energy balance and storage, and the effect of including freezing and thawing processes. The changes involve 1) the net effect of an improved soil physical representation and 2) the sensitivity of our results to changed soil parameter values and their contribution to the simulation of soil temperatures and soil moisture, both aspects being presented in the frame of an increased bottom boundary depth from 9.83 m to 1418.84 m. The implementation of water phase changes and supercooled water in the ground creates a coupling between the soil thermal and hydrological regimes through latent heat exchange. Momentous effects on subsurface temperature of up to ±3 K, together with soil drying in the high northern latitudes, can be found at regional scales when applying improved hydro-thermodynamic soil physics. The sensitivity of the model to different soil parameter datasets occurs to be low but shows important implications for the root zone soil moisture content. The evolution of permafrost under pre-industrial forcing conditions emerges in simulated trajectories of stable states that differ by $4-6\cdot10^{6}$ km^2 and shows large differences in the spatial extent of $10^{5}-10^{6}$ km^2 by 2100, depending on the model configuration.

Increasing the depth of a Land Surface Model. Part II: Temperature sensitivity to improved subsurface thermodynamics and associated permafrost response

N. J. Steinert* and J. F. González-Rouco

Department of Earth Physics and Astrophysics, Geosciences Institute IGEO (UCM-CSIC), Complutense University of Madrid, Madrid, Spain

P. de Vrese

Max Planck Institute for Meteorology, Hamburg, Germany

E. García-Bustamante

Research Center for Energy, Environment and Technology (CIEMAT), Madrid, Spain

S. Hagemann

Helmholtz-Zentrum Hereon, Geesthacht, Germany

C. Melo-Aguilar

Department of Earth Physics and Astrophysics, Geosciences Institute IGEO (UCM-CSIC), Complutense University of Madrid, Madrid, Spain

J. H. Jungclaus and S. J. Lorenz

Max Planck Institute for Meteorology, Hamburg, Germany

*Corresponding author: N. J. Steinert, normanst@ucm.es

ABSTRACT

The impact of various modifications of the JSBACH Land Surface Model to represent soil temperature and cold-region hydro-thermodynamic processes in climate projections of the 21st century is examined. We explore the sensitivity of JSBACH to changes in the soil thermodynamics, energy balance and storage, and the effect of including freezing and thawing processes. The changes involve 1) the net effect of an improved soil physical representation and 2) the sensitivity of our results to changed soil parameter values and their contribution to the simulation of soil temperatures and soil moisture, both aspects being presented in the frame of an increased bottom boundary depth from 9.83 m to 1418.84 m. The implementation of water phase changes and supercooled water in the ground creates a coupling between the soil thermal and hydrological regimes through latent heat exchange. Momentous effects on subsurface temperature of up to ±3 K, together with soil drying in the high northern latitudes, can be found at regional scales when applying improved hydro-thermodynamic soil physics. The sensitivity of the model to different soil parameter datasets occurs to be low but shows important implications for the root zone soil moisture content. The evolution of permafrost under pre-industrial forcing conditions emerges in simulated trajectories of stable states that differ by $4-6\cdot10^6\,\mathrm{km}^2$ and shows large differences in the spatial extent of $10^5-10^6\,\mathrm{km}^2$ by 2100, depending on the model configuration.

1. Introduction

Land Surface Model (LSM) components contribute to Earth System Models (ESMs) with the representation of the subsurface thermal and hydrological state that is important for a realistic land-climate interaction, and ultimately, for a realistic simulation of the coupling between the atmosphere, lithosphere and biosphere (Koster et al. 2006; Guo et al. 2006).

The interaction between the land and the rest of the Earth's climate system is characterized by surface and subsurface properties and processes. Those include energy, momentum and water exchange, as well as biogeochemical cycles, most notably the carbon cycle. Sensible and latent heat exchanges depend on the soil thermal and hydrological states that are the result of soil properties (e.g., soil types, roughness length) and their changes in biophysical and biogeochemical processes (e.g., Geiger 1965; Delworth and Manabe 1988; Dickinson 1995a,b; Brubaker and Entekhabi 1996; Koster et al. 2004), as well as on vegetation changes, snow cover dynamics, and biophysical/biogeochemical processes that influence land-atmosphere interactions (Bonan 1995, 2015; Seneviratne et al. 2010; Melo-Aguilar et al. 2018). In the absence of advection and convection, the subsurface thermodynamic state is determined by the vertical temperature distribution, heat diffusivity, and the interactions between the thermal and hydrological states through water phase changes in the ground (e.g., Carson and Moses 1963; Hillel 1998; Stieglitz and Smerdon 2007; Turcotte and Schubert 2014).

Because of its high mass and heat capacity, the soil represents a reservoir for energy. It affects carbon and water budgets governed by ground heat storage and energy exchange with the atmosphere. Although the soil energy budget is relatively small compared to the ocean, it is the second largest in the climate system (Levitus et al. 2012; Stocker et al. 2013; von Schuckmann et al. 2020). This reservoir is sensitive to changes in soil conditions under a changing climate, which has significant natural and socio-economic consequences (e.g., Anisimov et al. 2010; de Vrese et al. 2018).

Since heat and water transport and storage are strongly modulated by water, energy and momentum fluxes at the land surface, the realism in the simulation of subsurface thermo- and hydrodynamical processes is important in LSMs. Current-generation LSMs have experienced substantial progress by introducing more realistic physical processes (Flato et al. 2013). An influencing factor for improving the realism of the ground energy and water balance is the depth of the Bottom Boundary Condition Placement (BBCP; Warrilow 1986) used in LSMs. A full discussion on that is provided in a companion paper (González-Rouco et al. 2021). The BBCP establishes the depth at which a zero-flux condition ensures energy preservation in the system so that no heat is gained/lost across the bottom boundary, where the thermodynamic component in the LSM uses the BBCP to solve the heat transport according to the thermal diffusion equation (Carslaw and Jaeger 1959; Smerdon and Stieglitz 2006). The bulk of the current-generation ESMs and regional climate models have BBCPs at depths that range between 2 and 10 m (Cuesta-Valero et al. 2016; Burke et al. 2020) allocating limited space for subsurface processes and hence, land-climate feedbacks (González-Rouco et al. 2009). Depending on the timescale and amplitude of the surface temperature signal, the affected subsurface is deeper for signals with longer periods and larger temperature variation (Mareschal and Beltrami 1992; Pollack and Huang 2000). A BBCP too close to the surface is likely to corrupt the subsurface representation of heat propagation with depth and energy distribution on multiple timescales (Lynch-Stieglitz 1994; Sun and Zhang 2004; Smerdon and Stieglitz 2006; Stevens et al. 2007; MacDougall et al. 2008) and enhances ground temperature variations in the upper meters of the soil column. In contrast, a realistically deep BBCP spreads the energy into the depth with implications for energy storage and the surface energy balance

(González-Rouco et al. 2021). Therefore, the BBCP influences the available space for energy storage and its interactions with hydrology through changes in the temperature profile.

The vertical movement of groundwater occurs down to the bedrock level. Water storage is affected by the depth of roots and bedrock that regulate the range within which plants interact with soil moisture. Below the soil, the bedrock only hosts thermal exchange through heat conduction (e.g., Carslaw and Jaeger 1959; González-Rouco et al. 2021). Although water content does not extend to a large depth, it is influenced by heat conducted to and from the deeper subsurface. The conductive process in the soil can be modified if latent heat from water phase changes and soil moisture influence the soil thermal properties (Sorour et al. 1990). If the soil contains enough moisture, the energy from the freezing/thawing of soil water is present as latent heat flux (Woo 2012). The release/uptake of latent heat influences the soil and surface energy balance and affects the atmospheric circulation (Hagemann et al. 2016; Jaeger and Seneviratne 2011). Dry soils cannot release water, so that most of the incoming net energy is transferred via the sensible heat flux (Seneviratne et al. 2010). Particularly in high-latitude regions, the release of latent heat from melting or freezing soil moisture delays the change of soil temperatures commonly referred to as the zero-curtain effect (Outcalt et al. 1990). Thus, a realistic distribution of heat in the ground is relevant for near-surface and soil hydrology above the bedrock limit.

In the high latitudes, the upper part of the soil is characterized by a freeze-thaw cycle throughout the year, the so-called active layer. The soil below the active layer, at which temperatures stay below 0°C for at least two consecutive years, is defined as permafrost. Frozen soil thermodynamics are characterized by an exponential temperature attenuation from the surface propagating into the soil with a slope varying with the seasonal cycle (Carslaw and Jaeger 1959; Koven et al. 2013). The amount of latent heat used in phase changes of water in the active layer causes the surface temperature profile to attenuate stronger with depth than in the frozen soil below. The ground heat flux is governed by the temperature gradient between the ground surface and the permafrost, soil thermal properties, and surface cover factors such as vegetation or snow (Loranty et al. 2018).

Nowadays, permafrost is estimated to occupy 20–25 % of the Northern Hemisphere (NH) land (Brown et al. 2002; Zhang et al. 2008; Gruber 2012) and observations suggest that permafrost is reducing in spatial (horizontal and vertical) extent with anthropogenic warming (Jorgenson et al. 2001; Zhang et al. 2005). In turn, organic carbon (about 1672 Pg; Tarnocai et al. 2009) and soil nutrients that remained isolated from the global biogeochemical cycle for millennia (Froese et al. 2008) are getting released into the atmosphere through microbial organic matter decomposition from increased temperatures (Heimann and Reichstein 2008; Schuur et al. 2008; Koven et al. 2011) and arctic amplification due to the ice-albedo feedback (Manabe and Stouffer 1980). The degradation of permafrost causes positive feedback that accelerates climate change (e.g., Abbott and Jones 2015; Voigt et al. 2017). The expected potential carbon release from present permafrost soils amounts to 37–174 Gt (Schuur et al. 2015) by 2100 under an RCP8.5 climate trajectory. Further, a decrease in permafrost areas is important because the frozen soil underneath the active layer blocks the vertical movement of water (Bockheim 2015). With an extended active layer thickness, soil moisture is likely decreasing in this process, reducing the volume of soil water that is available for refreezing (Seneviratne et al. 2010).

It is also expected that, in a warming climate, the amount of snow-covered ground is reduced while increasing the area of soil exposed to the interaction with the atmosphere (Biskaborn et al. 2019; Soong et al. 2020; Bartlett 2004; Romanovsky et al. 2010; García-García et al. 2019). As snow has a strongly insulating effect, it builds a natural barrier between the ground and the air above, leading to a measurable offset in the coupling between ground and air temperatures (Pollack and Huang 2000; Beltrami and Kellman 2003; Stieglitz et al. 2003; Smerdon et al. 2004; Melo-Aguilar et al. 2018) and reduces the release of heat from the land into the atmosphere. With missing snow cover, atmospheric temperature changes can penetrate the ground and change the energy distribution in the climate subsystems. In turn, permafrost soils become more vulnerable to increasing surface temperatures. The duration and depth of snow cover influence the propagation of the air temperature signal into the ground and can lead to variations in the land-air temperature relationship at decadal (Bartlett 2005) and centennial (Melo-Aguilar et al. 2018) timescales.

The simulation of high-latitude soil dynamics in the Climate Model Intercomparison Project Phase 5 (CMIP5) models shows a wide range of results in both the present and future climate. Models often show substantial biases in hydrological variables over the high northern latitudes due to insufficiently realistic parameterizations of cold-region relevant processes such as soil-water freezing, soil moisture-ice feedback, and the representation of organic and snow layers (Paquin and Sushama 2015; Nicolsky et al. 2007; Swenson et al. 2012; Slater and Lawrence 2013; Koven et al. 2013). Koven et al. (2013) and Slater et al. (2017) found that simulated permafrost in CMIP5 LSMs mainly suffers from structural weaknesses in snow physics and soil hydrology. Burke et al. (2020) suggest that models should have a more refined and deeper soil profile to mitigate some of these biases, particularly the simulation of summer thaw depth. Large differences in the simulation of the cold-region climate and hydrology occur in different LSMs even with a comparable implementation of frozen ground physics (Luo et al. 2003; Andresen et al. 2020). These differences appear to be also influenced by the choice and characterization of the model parameters, initialization and boundary conditions (Sapriza-Azuri et al. 2018) since the spatial distribution of soil parameters is usually constant and predefined by look-up tables based on land cover and soil-type maps retrieved from sparse observations (Mendoza et al. 2015). Soil thermal parameters such as ground heat capacity and thermal conductivity are usually dependent on soil moisture storage and its variations in time (Abu-Hamdeh and Reeder 2000; Sorour et al. 1990; Loranty et al. 2018), which is not accounted for in many state-of-the-art LSMs (e.g., Flato et al. 2013).

This study investigates 1) the net effect of an improved physical representation of the coupling between soil hydrology and thermodynamics and 2) the sensitivity of our results to changed soil parameter values that include soil water storage space and root zone depth. Both aspects are presented in the frame of an increased BBCP-depth, which is addressed in detail in a companion paper (González-Rouco et al. 2021). In the first part of this paper (Sect. 2), the characteristics of the model and the simulations employed, as well as the hydro-thermodynamic changes used herein, are presented. Subsequently, Section 3 describes and discusses the results. Introducing a deeper BBCP aims to contribute to a more realistic representation of subsurface temperature (Sect. 3.a). Understanding the underlying dynamics that define the interaction between thermodynamic, hydrological and biogeophysical processes is crucial for a realistic subsurface representation. Thus, in Sections 3.b and 3.c, we explore the model sensitivity to individual physical processes under conditions of a deeper BBCP and assess their contribution to soil temperature and moisture changes. The influence of model changes on terrestrial energy storage is discussed in Section 3.d. Finally, we assess the simulated state and variability of permafrost in 21st-century scenario projections and use observations to verify the simulated spatial extent of permafrost in Section 3.e. Section 4 summarizes and concludes the main findings.

2. Model framework

a. The Land Surface Model

JSBACH version 3.20p1 (JSBACH hereafter; Reick et al. 2021) is the LSM component of the MPI-ESM (Giorgetta et al. 2013a; Stevens et al. 2013; Jungclaus et al. 2013; Mauritsen et al. 2019) used in CMIP6. JSBACH has been part of multiple evaluation studies as part of MPI-ESM (Hagemann et al. 2013; Hagemann and Stacke 2015), for JSBACH only (e.g., Ekici et al. 2014, 2015), and it has also been shown that JSBACH is a state-of-the-art LSM in several multi-model intercomparison studies (Burke et al. 2020; Essery et al. 2020; Menard et al. 2021). The horizontal resolution is T63 (roughly 1.85 degrees on a homogeneous grid). In the standard setup of JSBACH, the subsurface vertical structure is discretized in five layers, increasing unevenly in size with depth with a BBCP at 9.83 m (Roeckner et al. 2003). The boundary condition at the bottom of the lowest layer is defined by a zero heat flux. The subsurface vertical temperature profile is calculated by conduction following the heat conduction equation (Warrilow 1986). No convective and radiative heat transfer is considered. This study uses a vertically extended JSBACH with a deeper BBCP improving the simulated subsurface temperatures (see details in González-Rouco et al. 2021). The standard 5-layer configuration with a mid-layer depth of 0.03 m, 0.19 m, 0.78 m, 2.68 m and 6.98 m is kept and extended by seven additional layers with mid-layer depths of 15.71 m, 33.35 m, 68.42 m, 137.70 m, 274.07 m, 542.06 m and 1068.24 m. The corresponding layer bottom depths are shown in Figure 1 (also see Table 1 in González-Rouco et al. 2021). BBCP-depths are established at layer 5 (12) for the shallow (deep) hydro-thermodynamic structure. The geothermal heat flux is not considered in JSBACH as the effect on permafrost areas and carbon pools is expected to be small (Hermoso de Mendoza et al. 2020).

Increasing the depth of the BBCP is also relevant for the interaction with hydrological processes. JSBACH has a layered soil hydrology scheme (Hagemann and Stacke 2015), whose depth distribution follows that of the temperature discretization. The hydrology module allows for water to be stored down to the bedrock level and does not constrain soil moisture to the depth of the root zone. The soil moisture in the space between the root zone and the bedrock limit (soil moisture residue space, Fig. 2), which cannot be accessed by the plants for evapotranspiration, is more persistent against sudden changes (seasonal to climatic) at or near the ground surface and the annual hydrological cycle, and therefore represents an important buffer for soil moisture memory (Hagemann and Stacke 2015). However, since the occurrence of the soil moisture is limited by the bedrock level (Fig. 1), it depends on predefined values that are initially assigned to account for its geophysical distribution, as well as those of the root level and other relevant thermal parameters such as soil and rock specifications and their thermal properties of conductivity and diffusivity (Jackson and Taylor 1986; Sorour et al. 1990; Hagemann 2002). Most soil moisture activity is confined within the first 5 model layers except for minor contributions within the sixth layer in northern Eurasia (Fig. 2).

A representation of the vertical structure and basic fluxes in JSBACH is provided in Figure 1. The surface is insulated by an organic layer in forest areas. In snow-covered areas, JSBACH includes a snow model of varying complexity, depending on the model configuration (see Section 2.b). In the case of water phase changes, latent heat exchange is present, modulating the vertical heat and moisture fluxes. The root zone may exceed the active layer depth, especially in winter. Below the bedrock limit, there is heat transfer only. The soil carbon model (Goll et al. 2015) is not activated, and the JSBACH version used herein does not feature dynamic vegetation.

Simulated permafrost boundaries in JSBACH are obtained from estimated active layer thicknesses derived from simulated soil temperatures. The maximum thaw depth of any given year is defined as the largest depth of positive soil temperatures. Linear interpolation between the soil temperature at this layer and the layer below determines the approximate depth at which the interpolated line intersects the thawing/freezing point between the layer centers. We define permafrost to be present when the maximum active layer thickness is not deeper than 3 m (Lawrence and Slater 2005).

b. Soil hydro-thermodynamic coupling

In the standard JSBACH configuration (JSBACH-REF hereafter), freezing and thawing of soil water are not represented, and no latent heat exchange due to phase changes is present (correspondent to the model used in González-Rouco et al. 2021). That means that there is a decoupling of the thermal scheme from the soil hydrology. Ekici et al. (2014) improved the representation of cold-region physical soil processes in JSBACH-REF, leading to a simulation of more realistic soil conditions in permafrost areas as the soil hydro-thermodynamic coupling (HTC) allows for more realistic water states and movement (JSBACH-HTC hereafter; Fig. 1). HTC involves four particular changes: 1) freezing and melting of soil water, 2) allowance of supercooled water, 3) a five-layer snow model, and 4) moisture and time-dependent soil thermal properties such as heat capacity and thermal conductivity, all of which will be described in the following. Compare Figure 1 in González-Rouco et al. (2021), which coincides with JSBACH-REF, to Figure 1 herein to compare the differences in model features between JSBACH-REF and JSBACH-HTC.

In JSBACH-HTC, water may change its aggregate state with a freeze-thaw cycle and latent heat exchange (LHE; Fig. 1). A coupling between thermal and hydrological processes is reached through latent heat fluxes providing (consuming) energy when freezing/condensation (melting/evaporating) takes place. During the freeze-thaw cycles, it is optional whether supercooled water (SCW; Fig. 1) is active. When present, a portion of the soil water remains liquid below 0°C in a supercooled state and is accessible for plants (see details in Ekici et al. 2014). The formulation follows the freezing-point depression equation (Niu and Yang 2006), where the supercooled soil water at subfreezing temperatures is equivalent to a depression of the freezing point caused by a decrease in the water vapor pressure. A decrease in the vapor pressure leads to lowering the temperature at which the vapor pressures of ice and water are equal so that water can be in a supercooled liquid state. In JSBACH-REF, supercooled water is implicitly active because no phase changes are included so that water can stay liquid at temperatures below the freezing point. In snow-covered surface conditions (Roesch et al. 2001), hydrologically inactive layers of snow may add up to a maximum number of five (SNOW; Fig. 1) in JSBACH-HTC (Ekici et al. 2014). Snow piles up from the top layer, and while the bottom layer has an unlimited thickness, the other layers are up to 5 cm thick. The surface temperature forces the uppermost snow layer, while the lowermost layer forces the soil temperature profile. The snow layers contain no liquid water and there is no meltwater flux through the snowpack. However, moisture exchange from meltwater with the soil is accounted for in the hydrological scheme. The surface of JSBACH-HTC is insulated by an organic layer, which is not included in JSBACH-REF.

Additionally, JSBACH-HTC has different options to simulate soil thermal properties. In JSBACH-REF, the thermal conductivity and heat capacity are constant throughout the full model depth based on predefined values depending on soil types of the Food and Agriculture Organization of the United Nations dataset (FAO; Dunne and Willmott 1996). Although bedrock is prescribed for the hydrological regime, JSBACH-REF ignores the bedrock for heat transfer and uses thermal diffusivity values of the assigned FAO soil type for the entire ground column. In contrast to that, JSBACH-HTC uses a dynamical calculation of the heat capacity and thermal conductivity (DCC) based on the soil water content, porosity and density (Ekici et al. 2014; Johansen 1977; Loranty et al. 2018) for the soil down to the bedrock level. For the bedrock, JSBACH-HTC assigns a constant value for the thermal diffusivity of $1 \cdot 10^{-6}\,\mathrm{m^2 s^{-1}}$. It is important to understand the contribution of the individual HTC improvements with a deepened BBCP to understand their integral effect at multidecadal timescales. This also helps to assess potential improvements for state-of-the-art LSMs.

c. Initial and boundary conditions

Two different soil parameter datasets are used to initialize JSBACH. The first one (SPD1; Hagemann and Stacke 2015) is based on the Land Surface Parameters 2 dataset developed by Hagemann et al. (1999), Hagemann (2002) and improved FAO soil type dataset (K. Dunne, pers. Comm., 2005) based on FAO/Unesco (1971–1981). In line with improvements that have been developed with regard to the vertical structure of the hydrological module in JSBACH, a new derivation of the water holding capacity and volumetric field capacity was developed and, consequently, changes in the plant rooting depth were introduced (Hagemann and Stacke 2015). Soil parameter values in SPD1 that describe different soil textures used to compute various ground properties in JSBACH are summarized in Hagemann and Stacke (2015). The second soil parameter dataset (SPD2) is related to the development of the coupling between the thermal and hydrological schemes through latent heat exchange (Ekici et al. 2014). In SPD2, the soil depth, rooting depth, and the maximum moisture-holding capacity are modified from SPD1. It is a combination of the standard parameters (SPD1) and parameters from the Harmonized World Soil Database (HWSD). The specific soil type thermal properties are given in Ekici et al. (2014). Changes in the bedrock limit are based on the HWSD (FAO et al. 2009; Ekici et al. 2014).

Since JSBACH-REF does not consider moisture-dependent soil thermal properties, SPD-changes do not influence its simulations. Also, in JSBACH-REF, soil moisture changes do not produce feedbacks on temperature, as no heat-dependent water phase changes are simulated. For JSBACH-HTC, as moisture-dependence of the thermal properties and latent heat exchanges are included, the increase (decrease) in soil moisture leads to increased (decreased) vertically averaged thermal diffusivity and therefore enhances the conduction of surface temperatures into the ground. An increase (decrease) of moisture in the soil column is mainly related to the expansion (reduction) of the soil moisture residue space, either due to a decrease (increase) in root depth, an increase (decrease) in soil depth, or both at the same time. Latent heat exchanges may be affected in regions where there is an excess of heat to melt/evaporate soil moisture. The associated soil moisture changes influence the soil thermal properties and/or the soil temperatures conducted into the ground.

The purpose using these datasets is to investigate the model sensitivity of changes in the soil moisture associated with soil and root depth changes under deeper BBCP-conditions (Fig. 2). Soil moisture was shown to have a memory effect by being persistent against sudden changes (seasonal to climatic) at and near the land surface (Hagemann and Stacke 2015; Dirmeyer et al. 2009). In general, the presence of water in the land system produces important effects on the land energy and water balance in regions where vegetation processes control evapotranspiration (Lawrence et al. 2007; Hong et al. 2009; Forzieri et al. 2020; Guillevic et al. 2002). If the soil contains enough moisture, the energy from the phase change of soil water is present as latent heat flux (Woo 2012). Thus, water storage on land in the form of soil moisture, snow, and ice acts as an important memory component in the climate system (e.g., Koster and Suarez 2001; Seneviratne et al. 2006; Hagemann and Stacke 2015; Hagemann et al. 2016).

Figure 2 shows the spatial distribution of the rooting depth, soil depth, and soil moisture residue space for SPD1 and SPD2, respectively. Globally, the soil depth (bedrock limit) is generally less than 10 m. In some land grid points (0.36% for SPD1 and 0.02% for SPD2), the bedrock limit of SPD1 can exceed the BBCP-depth (9.83 m) of the standard shallow JSBACH. Extending the BBCP-depth at these grid points enables more soil moisture to be stored below layer 5 in the deep model configuration. A detailed description of JSBACH is also provided in González-Rouco et al. (2021). Since the roots are relatively shallow in this area, it makes for a large space of potential water storage. In SPD1, roots are generally deeper in the tropics and become more shallow towards the poles. The mid-to-high latitudes have relatively deep soil, which also raises the potential for water to reside there throughout the annual cycle. A direct comparison between SPD1 and SPD2 shows that rooting depth has been altered globally, with increases in the subtropics and major decreases in the tropical rain forest and desert areas (Fig. 2, right). Rooting depth changes in the NH high latitudes are relatively small. Soil depth in SPD2 has also been modified considerably with differences of up to ±5 m compared to SPD1. These large changes result in a similar pattern of soil moisture residue space differences. Mid latitudes experience large changes. At the high latitudes, absolute changes are smaller but still important in relative terms.

d. Experimental setup

JSBACH is used in the shallow five-layer and deep twelve-layer configurations. No intermediate level configurations with 6 to 11 layers are used as in González-Rouco et al. (2021). Simulations with three different radiative forcing scenarios are performed: 1) Pre-industrial control conditions (PIC); 2) historical conditions (HIS, 1850–2005) from anthropogenic forcing of greenhouse gases, atmospheric aerosols, volcanic ozone, and solar variability; and 3) representative concentration pathways (RCP, 2006–2100; van Vuuren et al. 2011) RCP8.5, RCP4.5, and RCP2.6 (Taylor et al. 2012). JSBACH is run with boundary conditions from PIC, HIS and RCP simulations from the coupled MPI-ESM. The RCP6.0 scenario is not included since no atmospheric forcing files for the standalone JSBACH exist from the CMIP5 MPI-ESM (e.g., Giorgetta et al. 2013b). An evaluation of the combined land-surface energy and water fluxes in the frame of the MPI-ESM for CMIP5 is given in Hagemann et al. (2013). PIC forcing conditions consist of a 28-year forcing interval that is repeated throughout the simulation. Initial conditions for HIS were derived from PIC simulations after 500 years when the simulation was sufficiently in equilibrium in the subsurface layers (González-Rouco et al. 2021). Those for RCP were started from HIS year 2005. With this setup, we perform simulations with the deep and shallow BBCP, SPD1 and SPD2, and HTC-off/on, respectively, resulting in eight experiments (Tab. 1). For different hydrological configurations of JSBAH-HTC, we perform four additional experiments.

3. Results and discussion

a. BBCP, SPD and HTC changes

In order to explore the influence of the BBCP changes on our results, we compare the shallow (5-layer) and deep (12-layer) configurations for all eight experiments. Results for the reference simulations REF_SPD1s and REF_SPD1d (Tab. 1) have been established in González-Rouco et al. (2021). However, incorporating changes in soil parameters and an improved physical representation of NH high-latitude hydro-thermodynamic processes used in the JSBACH-HTC experiments allows investigating the sensitivity of the LSM to these changes under the condition of a realistically deep BBCP. Figure 3 shows the direct comparison at layers 1–5 (0.03–6.98 m mid-layer depth) between the shallow and the deep model with respect to configuration changes (SPD1 vs. SPD2 and JSBACH-REF vs. JSBACH-HTC; see Table 1) in different forcing scenarios and latitudinal bands. There is a global mean cooling of 0.8–1.1 K by the end of the 21st century (average of 2071–2100) in the model with a deep BBCP for all configurations relative to the PIC simulation with a shallow LSM. The relative soil column cooling can be observed in all layers, increasing gradually with depth, and is largest at layer 5. The relative ground cooling can be explained by the downward transfer of heat from anthropogenic warming below the 5th layer in the deep model (González-Rouco et al. 2021). It also indicates overly strong warming of the soil column in the shallow 5-layer model. At these scales, model configuration changes have a relatively small influence on temperature differences. By incorporating hydro-thermodynamic soil coupling, the cooling is larger by about 0.2 K at layer 5. Changes in the soil parameter values result in no changes in JSBACH-REF but show less cooling when SPD2 is used in JSBACH-HTC. This is consistent for all forcing scenarios (not shown). Throughout the simulation, the temperature difference increases are fairly linear in the RCP8.5 scenario. The same is evident in the other scenarios. For the end of the 21st century, the strongest radiative forcing produces the largest response, with the relative cooling in RCP4.5 (RCP2.6) accounting for about half (a quarter) of that in RCP8.5 and enhancing by about one-tenth of a degree in JSBACH-HTC compared to JSBACH-REF. In comparison to the global mean, there is different strength in the temperature response to BBCP changes in different latitudinal bands (González-Rouco et al. 2021). In JSBACH-REF, the NH high latitudes have larger relative cooling at layer 5 than the global and low-to-mid latitude averages by 0.2–0.3 K. The Southern Hemisphere (SH) shows a weaker response in general. With respect to the soil parameter variations, there is some enhancement of the relative cooling of the SH mid-latitudes to NH mid-latitudes.

The spatial differences between the shallow and the deep JSBACH for all four configurations of HTC and SPD show the areas where the cooling is most prominent (Fig. 4). For the RCP8.5 forcing scenario, there is a general cooling all over the globe in the deep JSBACH-REF experiments. The largest cooling of up to 2 K can be found at layer 5 throughout the full band of NH high latitudes and in areas of Russia and South America in JSBACH-REF simulations, both with SPD1 and SPD2. The differences in the patterns resulting from SPD1 and SPD2 are significant but do not show large spatial variability. Incorporating coupled hydro-thermodynamic soil physics into the JSBACH-HTC simulation shows larger regional ground cooling distributed over central Eurasia, South Africa and across America. Predominantly, desert areas with low soil moisture are affected. Hence, no effect is expected with respect to including physical processes related to water phase changes. However, implementing a dynamic calculation of soil properties is responsible for a significant regionally intensified cooling since variations of thermal diffusivity throughout the soil column cause the temperature to distribute differently in the soil. Areas of intensified cooling are the result of higher thermal diffusivity, meaning that the temperature changes from the surface propagate faster into the soil (see more details in Section 3.c.2). In turn, the cooling of the ground in the deep model indicates an overestimation of soil temperatures in the shallow model. This relative warming in the shallow model is intensified in dry soil regions when soil thermal properties are set constant (JSBACH-REF). Although Ekici et al. (2014) targeted the improvement of high-latitude cold regions, we find differences and a potentially improved behavior over regions outside of those for which the soil hydro-thermodynamic coupling was made for in JSBACH-HTC.

b. Soil moisture and temperature sensitivity

Figure 5 shows the impact of HTC and SPD changes in the frame of deep and shallow BBCPs. The simulation of the absolute global average temperature of the HIS/RCP time series of the deep model shows a consistent increase in temperature throughout the length of the simulation for the surface temperature (Fig. 5; top). Surface warming has a strong influence on the first model layer. The temperature response is gradually decreasing throughout the soil downward. The amplitude of high-frequency fluctuations decreases and, by the end of the 21st century, the warming amplitude is gradually attenuated with depth. The warming signal from the surface is noticeable in deeper layers down to the 10th model layer (274 m mid-layer depth) but does not reach deeper layers, suggesting that the depth of the soil thermal scheme used herein is sufficiently deep to capture the warming signal of the RCP8.5 surface forcing.

Throughout the depth, the global mean soil temperature in the deep model varies slightly among the different configurations of HTC and SPD but follows, in general, the forcing imposed at the surface (Fig. 5; left). In the upper 20 m, the variation in the combinations of SPD and HTC configurations determines the detailed evolution of temperature in each layer. The influence of HTC is much larger than the influence of the selection of the parameter dataset. Apart from the first layer closest to the prescribed surface conditions, HTC causes the temperatures to be lower than the reference REF_SPD1d by 0.2–0.6 K, intensifying with depth. It reaches its maximum at layer 6 (≈16 m mid-layer depth). HTC increases the variability in the subsurface temperatures in comparison to the reference simulation REF_SPD1d. It appears to dominantly impact high-frequency temperature variations, as this temperature evolution discrepancy disappears below 10 m with respect to variability, and only an average temperature offset of a couple of tens of a degree is left. In JSBACH-REF, the influence of changing the soil parameter dataset is negligible. However, in JSBACH-HTC, SPD2-SPD1 temperature changes are of the order of 0.1–0.2 K, which adds on top of the HTC-influence in the HTC_SPD2s/d simulations. Still, the global variations in subsurface temperatures due to different physical representation (HTC) and soil parameters (SPD) are small compared to the temperature anomalies of 2100 with respect to 1850 in the RCP8.5 scenario that exceed an anomaly of 6–7 K (Fig. 5).

At regional scales, shown as latitudinal bands in the box plots in Figure 5, temperatures differ among different regions and physical configurations of the deep model. In general, the mid and high latitudes show larger anomalies with respect to pre-industrial conditions than the equatorial regions. Temperature differences between the model configurations are small compared to the temperature anomalies from 1850. However, regional average differences reach up to 2.2 K in the high northern latitudes. Further, NH high-latitude anomalies in JSBACH-HTC are higher than in JSBACH-REF. The range of temperatures of 2071–2100 in the low latitudes is larger than in other regions, which suggests either a higher range of variability or a stronger response of ground temperatures to the radiative forcing conditions in the last 30 years of the simulations in this area. Throughout the soil depth, the relative behavior of ground temperature anomalies for the various regions (top 5 layers) stays constant.

Specific regional patterns of the ground temperature response to the HTC and SPD configuration changes are shown in Figure 6. When using JSBACH-HTC, patches of significant warming and cooling areas occur compared to JSBACH-REF, mainly concentrated over NH land. Consistent warming is located over the full longitudinal width of the high northern latitudes, and in part of the Himalayan high mountain ridges (Fig. 6b). Dominating cooling patterns can be found in desert environments, such as the Sahara, the Arabian Peninsula and the Gobi region. The local temperature anomalies range between -3 K and 3 K, which is larger than the average global or latitudinal response of JSBACH-HTC. The origin of these patterns is discussed in Section 3.c. Furthermore, as seen from the time series in Figure 5, a change in SPDs has a negligible impact on the ground temperatures when using JSBACH-REF. However, in JSBACH-HTC, considerable patches of warmer temperatures occur in the NH mid-to-high latitudes in SPD2 compared to SPD1 (Fig. 6c).

Soil moisture content in the JSBACH root zone is larger in the equatorial regions, parts of western Asia and western North America (Fig. 6d). Dryer areas are located in desert areas of North Africa, Central Eurasia, and the higher latitudes. Introducing hydro-thermodynamic coupling in JSBACH-HTC reduces the absolute moisture content of land areas north of 45N significantly by more than 0.2 m on average, while the effect on the rest of the world is moderate to none (Fig. 6e). Liquid water that resides in the soil in JSBACH-REF is frozen in JSBACH-HTC when water phase changes are taken into account. This is visible in isolated patches of reduced moisture content in mountainous regions south of 45N, e.g., the Himalaya region. In terms of the influence of SPDs on soil moisture content (Fig. 6f), changes are distributed unevenly globally. However, there is no significant effect in the high latitudes. This is expected as there is larger terrestrial hydrological sensitivity in wet regions than in dry regions (Kumar et al. 2016). The global patterns correspond spatially with changes in the rooting depth between SPD1 and SPD2 (Fig. 2) since plant root depth affects soil water content significantly (e.g., Kleidon and Heimann 1998; Nepstad et al. 1994).

In high-latitude regions, evapotranspiration is limited by net radiation and the length of the growing season (Seneviratne and Stöckli 2008), which limits the amount of water used by the plants for photosynthetic growth. Apart from the deserts, equatorial regions predominantly show drier patches, while the subtropical bands of both hemispheres have wetter soils. In general, both changes of HTC and SPD imply important changes in the distribution of moisture in the soil. An increase in the depth of the bedrock limit increases the ability to store maximum soil moisture. Changes are of the magnitude of 50–100% on a regional scale and therefore potentially influence the soil properties and the ability of the soil to conduct energy into the depth. However, many near-surface processes rely on the relative soil moisture in the upper soil layers, which may remain relatively stable when increasing the bedrock limit.

The impact of the radiative forcing on the ground temperatures in the 21st century of the RCP8.5 scenario is strongest in the NH high latitudes because of arctic amplification (Fig. 7). The warming extends to 9 K in RCP8.5 with respect to the pre-industrial period in these regions. Continental areas experience slightly larger warming of 1–2 K compared to the coastal regions. The combined effect of activating HTC and changing to SPD2 (Fig. 7b) also shows the largest impact in the NH high-latitude regions with significant relative warming of up to 2 K in eastern Siberia. Meanwhile, the low and mid-latitudes of the NH experience regionally significant relative cooling in this configuration, particularly located at the central Eurasian continent and parts of western North America. The influence of model configuration changes reaches up to more than 2 K. This is a large difference, considering that the total temperature change from 1850–2100 is about 6–9 K regionally. There is substantial importance in the choice of the model configuration (see discussion in Section 3.c), which could impact the simulation results by an amount that is highly relevant for the discussion about climate change mitigation strategies and warming-limit agreements.

c. Contribution of soil coupling mechanisms

The soil temperature response pattern from Figure 6b can be explained by the contribution of different physical mechanisms taking part in JSBACH-HTC. Figure 8 shows the specific spatial patterns of each of the four physical mechanisms in HTC: 1) the use of 5 snow layers (SNOWon/off), 2) the use of the dynamic moisture-dependent calculation of soil thermal conductivity and capacity (DCCon/off), 3) the influence of soil water phase changes (LHEon/off) and 4) the implementation of supercooled water (SCWon/off). The maps correspond to the analysis of the 30-year long HTC_SNOW, HTC_DCC, HTC_LHE and HTC_SCW experiments in Table 1, in which one mechanism is being analyzed at a time. The influence of every mechanism has distinct regional signatures. A superposition of every single pattern may not entirely explain the final responses of soil temperature and moisture in JSBACH-HTC in Figure 6 because feedbacks and interactive processes occur.

In addition to the four contributing physical mechanisms in JSBACH-HTC, the thermal representation of bedrock differs in comparison to JSBACH-REF. However, 1) the changes in the diffusivity value between JSBACH-REF and JSBACH-HTC are small and their impact is negligible for the analysis presented herein (not shown), and 2) this merely affects the DDC-case because the other cases are using a comparison within different configurations of JSBACH-HTC, where the bedrock definition remains the same.

1) 5-layer snow scheme

Warming in the high northern latitudes is mainly caused by the insulating effect of snow cover. Spatial patterns of snow cover (Fig. 9a) agree well with the distribution of the soil temperature anomalies in Figure 8a in the high northern latitudes and the Himalaya region. The yearly evolution for surface temperature and soil temperature, as well as their differences at the site shown in Figure 8a (red dot), are shown in Figures 9b,c. Although snow depth is not subject to changes, a better representation of snow (SNOW) in the model configuration with the hydro-thermodynamic soil coupling (HTC_SNOW) leads the snow cover to act as a protective barrier for soil temperatures against colder air temperatures during winter. The insulation causes the annual mean soil temperatures to be higher than in the reference case without improved snow physics (REF_SPD1d). As long as the snow is present in the model between the first soil layer and the surface layer on top of the snow, soil temperatures are warmer. In spring, when air temperatures rise, the surface snow layer melts completely (Fig. 9c). In the first months, the soil temperatures are colder than the air because of the time lag of conductive coupling of the air temperatures with the soil. In summer, without a protective layer, the near-surface soil temperature follows the air temperature. Later in the year, when the snow starts to accumulate again, the insulating effect of the snow layer leads to a difference in air-soil temperatures (Fig. 9b). Therefore, SNOW introduces an increase in the first layer of soil temperatures in winter.

2) Dynamic soil thermal properties

Incorporating a dynamic calculation (DCCon; =HTC_SPD1d; Tab. 1) of thermal conductivity (k) and heat capacity (C) into the JSBACH results in colder temperatures by a couple of degrees compared to DCCoff (=HTC_DCC; Tab. 1) in some regions (Fig. 8b). From the distribution of soil moisture in the model (Fig. 6d) it is evident that this response is limited to areas with low soil moisture in the mid-latitudes. These are the areas showing a major change in k and C (Figs. 10a,b). The regions in the high northern latitudes (Siberia, Canada, Alaska), as well as the Himalaya region, have very shallow soil depth (Fig. 2) and thus contain a considerable amount of soil moisture relative to the soil depth and can be ignored here. Heat capacity values in DCCoff are overestimated in some humid areas and specifically in the arid regions because the predefined

(FAO-maps) values of C in DCCoff are larger than the dynamic C (Fig. 10a) that takes into account the soil moisture and ice content as well as the soil porosity in DCCon (Rempel and Rempel 2016; Loranty et al. 2018).

In arid regions, solar radiation is heating the surface during the day. The amount of incoming energy is the same in DCCon as in DCCoff, but in DCCon, the heat taken up by the surface layer cannot be transported away into deeper soil layers as quickly as in DCCoff because of the decreased thermal conductivity. This is visible in a decreased ground heat flux in DCCon between the 1st and 2nd soil layers (Fig. 10d). The temperature increase at the surface leads to increased sensible heat flux into the atmosphere during the day. At night, the soil is radiating outward and cools down, getting colder than the air above the ground and the sensible heat flux gets reversed such that the atmosphere now heats the soil. Generally, the deeper soil layers are now warmer than the surface, which results in an upward directed ground heat flux. The heat source from below is lower in DCCon than in DCCoff because less heat was stored into the lower layer during the day (and over many days), which could now 'fuel' the surface layer to equilibrate the radiative energy loss. Excessive loss of energy during the night leads to a net reduction of radiation during the night of up to $50\,\mathrm{W/m^2}$ (Fig. 10d). The result is a colder mean state of the soil in DCCon with larger variability in the diurnal cycle of sensible heat flux and temperature visible in the soil temperature profile (Fig. 10e). The surface energy partitioning is almost entirely defined by the sensible heat flux, as the available soil moisture and air-water contents are very low. The results are consistent with Wang et al. (2016), who find that a moisture-dependent parameterization of the soil thermal properties can be responsible for relative cooling in dry areas, and they conclude that this potentially affects the range of diurnal and intra-annual extreme temperatures.

In humid regions, as long as enough soil moisture is present in the soil, the balance between moisture-time-dependent heat capacity and heat conductivity adjusts so that soil temperatures are almost equal in DCCon and DCCoff. A particular role is played by the increased moisture-dependent heat conductivity in the DCCon, as sub-diurnal relative (DCCon vs. DCCoff) heat gain or heat loss can be distributed throughout the soil quickly. The ground heat flux is increased, suggesting that the excess energy is passed through to deeper layers (not shown). Large parts of surface energy are consumed/released for the phase change of soil and air moisture in the form of latent heat. Thus, humid regions are prone to regulate their latent heat flux according to the available energy in the soil that results from the dynamic moisture-time-dependent thermal conductivity and heat capacities, leaving the sensible heat fluxes almost indifferent between the two DCC configurations.

3) Latent heat exchange

In comparison to JSBACH-REF, JSBACH-HTC has colder soil temperatures in the annual average in the mid-latitudes (Figs. 6b; 8c), which can be related to the incorporation of soil freezing and melting process and according to latent energy exchange (LHE, Fig. 11) in the LHEon configuration (=HTC_SPD1d; Tab. 1). There is a seasonal behavior in the mid-latitudes that causes major warming in LHEon in winter (DJF) and a reversed cooling in summer (JJA), which balance each other out to an average response as seen in Figure 8c. In winter, ice is forming in LHEon, which is thawing in summer (Figs. 11c–e). In the example grid point, the soil ice at layer 2 is thawed completely in summer and exceeds the reference of LHEoff (=HTC_LHE; Tab. 1) in winter. Meanwhile, in LHEoff, the soil water content is constantly solid throughout the year, also in summer when the soil temperature is much higher than the water freezing point. Accordingly, the liquid soil water content in LHEon oscillates along with the seasonal soil temperatures. The freezing of soil water to ice in autumn and winter releases latent energy that warms up the soil and results in warmer soil temperatures in LHEon in winter (Figs. 11c–e). Reversely, latent energy is consumed to melt the soil ice in spring and summer and contributes to a colder soil state. From March to June (November to February), the zero-curtain effect is visible in the soil temperatures, which causes a lag of warming (cooling) in spring (autumn). Additionally, the phase change of soil water in LHEon affects the thermal properties of the soil. More ice content in winter increases the soil thermal conductivity, leading to more energy transported from the surface to deeper soil layers. At the same time, with the increase in liquid soil water content in summer, the heat capacity decreases, which further contributes to summer cooling. The increased water content causes almost a doubling of summer evapotranspiration (not shown) that further cools the ground surface. This cooling dominates the annual cycle in the soil temperature profile in the top 5 soil layers ($\sim$10 m), which results in a colder soil climate state on longer timescales (Fig. 8) and affects the average temperature in Figure 6.

4) Supercooled water

Similar to the mechanisms of the LHE case are those taking place in the presence of supercooled water (SCW, Fig. 12). As in LHE, there is a seasonal oscillation of near-surface soil temperature response to implementing supercooled water into the model. SCWon (=HTC_SCW) causes a predominant cooling pattern in the mid-latitudes in winter (DJF) and a reversed warming in summer (JJA, Figs. 12a,b). With SCWon, a portion of the water to be frozen when soil temperatures drop below zero degrees are kept in liquid form to be available for surface evapotranspiration. Thus, in winter, SCWon has water left in the soil, while in SCWoff (=HTC_DCC), it is completely frozen (Fig. 12c–e). The reduction of soil water frozen to ice in winter is equal to a reduction of latent heat released by the water phase change and results in less latent warming of the soil in SCWon. Reversely, in summer, less energy is consumed for the melting process of ice and leads to warmer soil temperature than in SCWoff. This leaves the SCWon simulation with a larger amplitude of the annual cycle. Although small, differences between SCWon and SCWoff in the annual maximum and minimum temperatures of the soil profile show slight domination of the winter cooling effect throughout the soil, leading to a colder soil in the annual average as seen in Figure 8, contributing slightly to the spatial pattern of temperature in Figure 6.

d. Terrestrial energy in future scenarios

Although the ground shows relative cooling when deepening the BBCP in JSBACH, e.g., lower warming relative to the shallow model (Fig. 3), energy is propagated and stored in the subsurface (González-Rouco et al. 2021). The heat from the land surface, imposed by net positive radiative forcing, is distributed into deeper layers in the deep model. The rate of energy uptake in the shallow and the deep model is compared in Figure 13 also in the frame for HTC and SPD influences. The deep model consistently stores more heat in the subsurface than the shallow model in all forcing scenarios. The intensity of the forcing contributes to the amount of energy stored. The largest energy gain is evident in the NH high-latitudes with a range of up to $10 \cdot 10^5 \mathrm{Jm}^{-2}\mathrm{yr}^{-1}$ (Fig. 13; blue labels), depending on the model configuration, in the RCP8.5 scenario. In contrast to the rest of the world, the NH high latitudes show a large difference in the amount of heat storage depending on whether HTC is used or not. In all forcing scenarios, RCP2.6, RCP4.5 and RCP8.5, the deep JSBACH-HTC simulations (Fig. 13; blue triangle and circle) reach differences of 10–20% relative to JSBACH-REF (Fig. 13; blue square and plus), which accounts for more than the total amount of energy storage in the shallow model configuration. Energy storage in the deep model is 7–9 times higher than in the shallow model for RCP8.5. Surprisingly, the relative rate of heat storage in RCP4.5 and RCP2.6 reaches between 10–14 times and 16–23 times the amount of storage in the shallow model, respectively. That means that the relative rate of subsurface heat storage per Kelvin in the low-to-moderate forcing scenarios is larger than in the business-as-usual scenario within a land surface model with a sufficiently deep BBCP. Apart from the high northern latitudes, the differences in the rate of terrestrial heat storage between the different configurations of HTC and SPD are relatively small. However, there is a clear dependence on the energy storage rate to the latitudinal bands.

e. Permafrost simulation and stability

The given changes in the thermal state of the soil in JSBACH under different model configurations impact the evolution of permafrost extent in the NH north of 45N. Permafrost areas are stable under pre-industrial climate forcing conditions and are reduced by the warming of surface temperature in the 20th to 21st century (Fig. 14). In conditions of a stable pre-industrial climate, permafrost extent evolves into two different stable states depending on the use of the soil hydro-thermodynamic coupling (JSBACH-HTC vs. JSBACH-REF). After starting from similar initial conditions in PIC, the JSBACH-HTC simulations transit into a different stable state than the JSBACH-REF simulations throughout the first decades (Fig. 14a). The two mean PIC states of permafrost extent range from about $12 \cdot 10^6\,\mathrm{km}^2$ (JSBACH-REF) to $19 \cdot 10^6\,\mathrm{km}^2$ (JSBACH-HTC), and their difference is about $4-6 \cdot 10^6\,\mathrm{km}^2$. At this stage, the JSBACH-HTC simulations are relatively close to recent estimates of observations of $17.8 \cdot 10^6\,\mathrm{km}^2$ (Hugelius et al. 2014) and $15.5 \cdot 10^6\,\mathrm{km}^2$ (Chadburn et al. 2017) and compare well to CMIP6 model estimates that vary between $10-20 \cdot 10^6\,\mathrm{km}^2$ (Burke et al. 2020). With JSBACH-REF, the simulations with different SPDs produce very similar permafrost extent, whereas, with JSBACH-HTC, the spread of simulations with different SPDs is larger. Natural variability is enhanced in the JSBACH-HTC-state and the response to the 28-year piControl driving cycle is not as regular anymore as in JSBACH-REF (González-Rouco et al. 2021). With JSBACH-HTC, the shallow model produces a larger areal extent of permafrost independent of the SPD. The differences between the shallow and deep JSBACH are comparably small but still in the order of 10^5km^2, relevant at regional scales.

After 1850, when the climate forcing conditions of the historical and RCP8.5 simulations lead to a warming of the ground surface temperature of about 7 K globally and up to 9 K in the high northern latitudes by 2100 (Fig. 5d), the permafrost is reduced by 30–50% by 2050 and 85–90% by 2100 (Fig. 15). Within the RCP4.5 scenario, permafrost loss is not as large, but permafrost constantly reduces until 2075. After that, it remains at a level of 30–45% of the pre-industrial permafrost extent. In RCP2.6, permafrost areas decrease moderately until 2045, transitioning to zero net emissions when the extent starts recuperating between 2045 and 2100. All three scenarios follow well the general evolution of ground temperatures (Fig. 5). The permafrost loss under future climate change conditions results in 1.5 and $2.3 \cdot 10^6$ km^2/°C for JSBACH-REF and JSBACH-HTC, respectively, with JSBACH-HTC being in better agreement to CMIP6 model estimates of $1.7 - 2.7 \cdot 10^6$ km^2/°C (Burke et al. 2020). It is apparent that among the different climate forcing scenario intensities, the evolution of permafrost extent is very similar until the middle of the 21st century (as it is for temperatures), and only after that, they diverge. Two different states of permafrost extent remain among the different model configurations for the full length of the simulations. Both states are driven down notably by the RCP4.5 and RCP8.5 scenario warming by 2100. However, their percentage difference increases by the end of the simulation, as seen from the slope of the decreasing permafrost extent in Figure 14 (b–d).

JSBACH-HTC has permafrost areas reaching out further to lower latitudes (Fig. 14e,f). During the historical period and by the end of the RCP2.6 scenario simulation, the differences between JSBACH-HTC and JSBACH-REF are noticeable. Although the soil column temperatures in the high-latitudes are warmer on an annual average (Fig. 6b), permafrost extends further south, particularly in Eurasia. The warming primarily stems from the insulating snow cover (Fig. 8).

However, in summer, colder temperatures dominate due to the implementation of water phase changes (Fig. 11b) and enhanced evapotranspiration. Since permafrost is defined by the summer maximum active layer depth that is decreased in JSBACH-HTC, permafrost extent decreases less in the 21st century for JSBACH-HTC. Towards more intense radiative forcing conditions in RCP4.5 and RCP8.5, the permafrost extent decreases in JSBACH-REF (47–49% and 91–93%, respectively; Fig. 15), while the generally larger permafrost area in JSBACH-HTC (Fig. 14f) experiences a lower decrease (41–47% and 85–88%, respectively; Fig. 15). Even in RCP8.5, where almost no permafrost is left in JSBACH-REF (Fig. 15), JSBACH-HTC shows noticeable permafrost areas. These differences are prominent and show that the implementation of more realistic hydro-thermodynamic soil physics is crucial for regional and global simulations of permafrost extent. They illustrate a high sensitivity of JSBACH to configuration changes, which could alter the spread and the equilibrium state of permafrost in comparable LSMs, as they have shown to be sensitive to configuration changes (e.g., Koven et al. 2013; Slater and Lawrence 2013; Sapriza-Azuri et al. 2018).

4. Summary and conclusions

In this paper, we examine the importance of various configurations of the JSBACH Land Surface Model to represent of soil temperatures and cold-region hydro-thermodynamic processes. These configurations involve 1) a deeper bottom boundary condition (González-Rouco et al. 2021), 2) two different soil parameter sets with the focus on soil moisture availability and spatial (also vertical) distribution, and 3) the implementation of various soil hydro-thermodynamic physical processes, which were introduced to JSBACH by Ekici et al. (2014), and their contribution to the representation of soil temperatures and soil moisture. The latter includes water phase changes, dynamic calculation of soil thermal properties, allowance for supercooled water, and a more elaborate 5-layer snow scheme. The hydro-thermodynamic parameterizations have been incorporated in other models before, but the simultaneous use of a deepened bottom boundary in an LSM as provided in this study adds novel insights into the ground thermodynamic processes and their relation with soil hydrology. The results emphasize the sensitivity of current state-of-the-art LSMs to the model configuration, including crucial physical processes and the choice of soil-property datasets. This is particularly true for simulations focusing on and including cold-region physics, as those regions are subject to changes under a warming climate.

With prescribing a deeper BBCP in the soil model under transient climate conditions, relative ground temperatures are reduced, providing evidence for shallow LSMs to have unrealistic relative warming. High magnitudes of this warming of up to 2 K can be found in the NH high latitudes (for a more detailed discussion, see González-Rouco et al. 2021). Introducing hydro-thermodynamic coupling contributes to even larger temperature differences between the deep and the shallow model at a regional scale. Additionally, there are large changes in the amount of terrestrial energy storage in climate warming scenarios. The land heat uptake increases by a factor of 7–26 with a more realistic soil model depth, depending on the forcing scenario and model setup. The deep model sensitivity to HTC can exceed the overall heat storage capacity of the shallow model, particularly in the high northern latitudes. Absolute numbers are still small in comparison to the ocean heat uptake but are considerably large in relation to the other Earth subsystems (von Schuckmann et al. 2020). Therefore, the energy missing in shallow LSMs is expected to be transferred to other climate subsystems, e.g., the atmosphere, when the BBCP is too shallow. This potentially results in a misrepresentation of the distribution of energy in coupled ESM simulations.

The sensitivity of JSBACH to using the hydro-thermodynamic soil coupling and changes in the soil parameters related to soil moisture availability is visible in the representation of ground temperatures and soil moisture content alike. JSBACH-HTC shows a 0.2–0.6 K cooling relative to

JSBACH-REF over central Eurasia, South Africa, and across America. Smaller relative warming is found when using an adapted soil parameter dataset SPD2. It also seems to trigger increased high-frequency variability. In general, the NH high latitudes appear to be the most sensitive to climate change and changes in the model configurations of HTC and SPD. These areas are also subject to substantial variations in strong future warming when SPDs are changed. Particular temperature responses to model configuration changes can be tracked by physical mechanisms that contribute to the warming and cooling patterns of JSBACH-HTC by a superposition of its individual components. The warming pattern in the NH mid-to-high latitudes comes from a better insulating snow cover. Cooling patches in low moisture desert areas stem from a dynamic calculation of soil thermal conductivity and heat capacity. The latter also provokes an increase in the diurnal temperature cycle in arid regions. The incorporation of water phase changes and supercooled water has a seasonally oscillating signal that contributes to net cooling in JSBACH-HTC. With respect to soil moisture content, an influence on the global scale can be seen from an alteration in the depth of the roots, which ultimately influences the amount of soil water that resides in the space between the root zone and the bedrock limit. The water residue acts as a buffer to short-term temperature variations at the surface and has a momentous impact on the soil properties for the conduction of heat into the soil. Furthermore, the water phase changes of JSBACH-HTC contribute to a different amount of liquid water that is available for plants during the cold NH winter season. Regional differences in the soil moisture content are as large as 100% compared to the reference. Thus, both HTC and SPD imply significant changes in the distribution and availability of moisture in the soil.

By including the improved hydro-thermodynamic soil coupling, the capability of our LSM to simulate permafrost is enhanced. Water phase changes and a more elaborate snow model are crucial for the soil thermal representation near the surface and in the deeper soil on a large spatial scale. The simulated permafrost is most sensitive to changes in the soil hydro-thermodynamic coupling, for which the model simulates two different states that are in the range of observational and model estimates (Hugelius et al. 2014; Chadburn et al. 2017). Natural variability of permafrost extent is enhanced under conditions of JSBACH-HTC. Both states are massively reduced by the end of the 21st century under the RCP4.5 and RCP8.5 scenarios, while their rate of permafrost degradation slightly differs. In RCP2.6, there is a moderate decrease in permafrost extent until 2045. After that, it recovers its permafrost to a larger area, while in the JSBACH-HTC simulations, it reaches back to a state under historical conditions in some areas. In the upper 10 m of the soil column, the impact of a deep soil model on the permafrost extent is relatively small but is expected to play a larger role when taking into account hydro-thermodynamic processes in larger depth down to 50 m (Hermoso de Mendoza et al. 2020). In both cases, the HTC-switches and BBCP-depth changes, differences in the extent of permafrost of the order of $10^5 - 10^6\,\mathrm{km}^2$ are crucial for estimating a potential release of carbon captured in the frozen ground.

This study neither simulates the evolution of terrestrial carbon stock nor a dynamic vegetation response. However, a rough estimation of the changes in the soil carbon release under climate warming conditions and its sensitivity to the modifications in JSBACH presented herein can be based on other studies on the permafrost-carbon climate feedback (e.g., Schuur et al. 2015). Considering the amount of carbon estimated to be stored in global permanently frozen soils, a proper representation of permafrost areas and their extent is crucial for the simulation of the climate system. A release of this carbon from the soil into the atmosphere fuels global climate warming by a potential enhancement of human-induced greenhouse gases by 22–40% (Comyn-Platt et al. 2018). Therefore, a quantitative estimation of soil carbon fluxes is desirable, but not done in the JSBACH-HTC version used herein, as the terrestrial vegetation and soil carbon pools usually have a long time lag to climate changes of multiple hundreds of years (e.g., Sentman et al. 2011; Scholze et al. 2003).

Additionally, in JSBACH-HTC, soil respiration is dependent on surface temperature and precipitation, rather than soil moisture and soil temperature. The former is defined by the surface entirely, which is subject to surface forcing in our standalone simulation setup and is unlikely to change realistically among our sensitivity analysis. Coupling with the atmosphere is needed to ensure the dynamic surface condition and more realistic coupling between land and atmosphere. A qualitative statement is still possible considering the amount of carbon stock of $17{\cdot}10^{14}$ kg CO_2 equivalent at present (Tarnocai et al. 2009) stored in $\sim 12 \cdot 10^6$ km^2 of permafrost land area. At the same time, 30% of the carbon emissions stem from permafrost areas in projections of the RCP8.5 forcing scenario by the time the simulated global mean temperatures increase by 2°C (MacDougall et al. 2015). With respect to the sensitivity of JSBACH-HTC in simulating permafrost areas under different model configurations and soil parameter datasets, an uncertainty of $6.6{\cdot}10^{14}$ kg of carbon release results from the spread in permafrost presented herein. This accounts for 158% and 57% of the global carbon emission targets of the 2016 Paris Agreement for 1.5°C and 2°C, respectively (Masson-Delmotte et al. 2018, 2019). The net carbon loss is expected to be less dramatic as there is also an increase in carbon uptake due to arctic greening (Berner et al. 2020). However, the sensitivity of our results for the simulation of permafrost illustrates the importance of a proper representation of high-latitude region soil physics.

Acknowledgments. We gratefully acknowledge the IlModelS project, project no. CGL2014-59644-R and GReatModelS, project no. RTI2018-102305-B-C21. Stefan Hagemann contributed in the frame of the ERANET-plus-Russia project SODEEP (Study Of the Development of Extreme Events over Permafrost areas) supported by BMBF (Grant no. 01DJ18016A). This work used resources of the Deutsches Klimarechenzentrum (DKRZ) granted by its Scientific Steering

Committee (WLA) under project ID bm1026. We wish also to thank Veronika Gayler for technical support on JSBACH.

Data availability statement. The JSBACH simulation data and soil parameter datasets used in this study are available from the corresponding authors upon reasonable request. They are available at the servers of the Deutsches Klimarechenzentrum (DKRZ) and need to be granted access by the authors and the DKRZ.

References

Abbott, B. W., and J. B. Jones, 2015: Permafrost collapse alters soil carbon stocks, respiration, CH4 , and N2O in upland tundra. *Global Change Biology*, **21 (12)**, 4570–4587, doi:10.1111/gcb.13069.

Abu-Hamdeh, N. H., and R. C. Reeder, 2000: Soil Thermal Conductivity Effects of Density, Moisture, Salt Concentration, and Organic Matter. *Soil Science Society of America Journal*, **64 (4)**, 1285–1290, doi:10.2136/sssaj2000.6441285x.

Andresen, C. G., and Coauthors, 2020: Soil moisture and hydrology projections of the permafrost region – a model intercomparison. *The Cryosphere*, **14 (2)**, 445–459, doi:10.5194/tc-14-445-2020.

Anisimov, O., and Coauthors, 2010: Major natural and social-economic consequences of climate change in the permafrost region: predictions based on observations and modeling. *Greenpeace*, 44 pp.

Bartlett, M. G., 2004: Snow and the ground temperature record of climate change. *Journal of Geophysical Research*, **109 (F4)**, doi:10.1029/2004jf000224.

Bartlett, M. G., 2005: Snow effect on North American ground temperatures, 1950-2002. *Journal of Geophysical Research*, **110 (F3)**, F03 008, doi:10.1029/2005JF000293.

Beltrami, H., and L. Kellman, 2003: An examination of short- and long-term air-ground temperature coupling. *Global and Planetary Change*, **38 (3-4)**, 291–303, doi:10.1016/S0921-8181(03)00112-7.

Berner, L. T., and Coauthors, 2020: Summer warming explains widespread but not uniform greening in the Arctic tundra biome. *Nature Communications*, **11 (1)**, doi:10.1038/s41467-020-18479-5.

Biskaborn, B. K., and Coauthors, 2019: Permafrost is warming at a global scale. *Nature Communications*, **10 (1)**, 264, doi:10.1038/s41467-018-08240-4.

Bockheim, J. G., 2015: *Cryopedology*. Progress in Soil Science, Springer International Publishing.

Bonan, G. B., 1995: Land-Atmosphere interactions for climate system Models: coupling biophysical, biogeochemical, and ecosystem dynamical processes. *Remote Sensing of Environment*, **51 (1)**, 57–73, doi:10.1016/0034-4257(94)00065-U.

Bonan, G. B., 2015: *Ecological Climatology: Concepts and Applications*. 3rd ed., Cambridge University Press, Cambridge.

Brown, J., O. Ferrians Jr., J. Heginbottom, and E. Melnikov, 2002: Circum-Arctic map of permafrost and ground-ice conditions, Version 2. USGS Numbered Series, NSIDC: National Snow and Ice Data Center, Boulder, Colorado USA.

Brubaker, K. L., and D. Entekhabi, 1996: Analysis of Feedback Mechanisms in Land-Atmosphere Interaction. *Water Resour. Res.*, **32 (5)**, 1343–1357, doi:10.1029/96WR00005.

Burke, E. J., Y. Zhang, and G. Krinner, 2020: Evaluating permafrost physics in the Coupled Model Intercomparison Project 6 (CMIP6) models and their sensitivity to climate change. *The Cryosphere*, **14 (9)**, 3155–3174, doi:10.5194/tc-14-3155-2020.

Carslaw, H., and J. Jaeger, 1959: *Conduction of Heat in Solids*, Vol. 1. Clarendon Press, Oxford.

Carson, J. E., and H. Moses, 1963: The Annual and Diurnal Heat-Exchange Cycles in Upper Layers of Soil. *J. Appl. Meteor.*, **2 (3)**, 397–406, doi:10.1175/1520-0450(1963)002<0397:TAADHE>2.0.CO;2.

Chadburn, S. E., E. J. Burke, P. M. Cox, P. Friedlingstein, G. Hugelius, and S. Westermann, 2017: An observation-based constraint on permafrost loss as a function of global warming. *Nature Climate Change*, **7 (5)**, 340–344, doi:10.1038/nclimate3262.

Comyn-Platt, E., and Coauthors, 2018: Carbon budgets for 1.5 and 2°C targets lowered by natural wetland and permafrost feedbacks. *Nature Geoscience*, **11 (8)**, 568–573, doi:10.1038/s41561-018-0174-9.

Cuesta-Valero, F. J., A. García-García, H. Beltrami, and J. E. Smerdon, 2016: First assessment of continental energy storage in CMIP5 simulations. *Geophys. Res. Lett.*, **43 (10)**, 2016GL068 496, doi:10.1002/2016GL068496.

de Vrese, P., T. Stacke, and S. Hagemann, 2018: Exploring the biogeophysical limits of global food production under different climate change scenarios. *Earth System Dynamics*, **9 (2)**, 393–412, doi:10.5194/esd-9-393-2018.

Delworth, T. L., and S. Manabe, 1988: The Influence of Potential Evaporation on the Variabilities of Simulated Soil Wetness and Climate. *J. Climate*, **1 (5)**, 523–547, doi:10.1175/1520-0442(1988)001<0523:TIOPEO>2.0.CO;2.

Dickinson, R. E., 1995a: Land-atmosphere interaction. *Rev. Geophys.*, **33 (S2)**, 917–922, doi:10.1029/95RG00284.

Dickinson, R. E., 1995b: Land processes in climate models. *Remote Sensing of Environment*, **51 (1)**, 27–38, doi:10.1016/0034-4257(94)00062-R.

Dirmeyer, P. A., C. A. Schlosser, and K. L. Brubaker, 2009: Precipitation, recycling, and land memory: An integrated analysis. *Journal of Hydrometeorology*, **10 (1)**, 278–288, doi:10.1175/2008JHM1016.1.

Dunne, K. A., and C. J. Willmott, 1996: Global Distribution of Plant-Extractable Water Capacity of Soil. *Int. J. Climatol.*, **16 (8)**, 841–859, doi:10.1002/(SICI)1097-0088(199608)16:8<841::AID-JOC60>3.0.CO;2-8.

Ekici, A., C. Beer, S. Hagemann, and C. Hauck, 2014: Simulating high-latitude permafrost regions by the JSBACH terrestrial ecosystem model. *Geoscientific Model Development*, **7**, 631–647, doi:10.5194/gmd-7-631-2014.

Ekici, A., and Coauthors, 2015: Site-level model intercomparison of high latitude and high altitude soil thermal dynamics in tundra and barren landscapes. *The Cryosphere*, **9 (4)**, 1343–1361, doi:10.5194/tc-9-1343-2015.

Essery, R., and Coauthors, 2020: Snow cover duration trends observed at sites and predicted by multiple models. *Cryosphere*, **14 (12)**, 4687–4698, doi:10.5194/tc-14-4687-2020.

FAO, IIASA, ISRIC, ISS-CAS, and JRC, 2009: *Harmonized World Soil Database (version 1.1)*. FAO, Rome, Italy and IIASA, Laxenburg, Austria,.

FAO/Unesco, 1971–1981: *Soil Map of the World*. Vols 1-10, Unesco, Paris.

Flato, G., and Coauthors, 2013: Evaluation of Climate Models. In: Climate Change 2013: The Physical Science Basis. Contribution of Working Group I to the Fifth Assessment Report of the Intergovernmental Panel on Climate Change. *Climate Change 2013*, Vol. 5, Cambridge University Press, 741–866.

Forzieri, G., and Coauthors, 2020: Increased control of vegetation on global terrestrial energy fluxes. *Nature Climate Change*, **10 (4)**, 356–362, doi:10.1038/s41558-020-0717-0.

Froese, D. G., J. A. Westgate, A. V. Reyes, R. J. Enkin, and S. J. Preece, 2008: Ancient permafrost and a future, warmer arctic. *Science*, **321 (5896)**, 1648, doi:10.1126/science.1157525.

García-García, A., F. J. Cuesta-Valero, H. Beltrami, and J. E. Smerdon, 2019: Characterization of Air and Ground Temperature Relationships within the CMIP5 Historical and Future Climate Simulations. *Journal of Geophysical Research: Atmospheres*, **124 (7)**, 3903–3929, doi:10.1029/2018JD030117.

Geiger, R., 1965: *The climate near the ground.*, Vol. 93. Harvard Univ. Press, Camebridge.

Giorgetta, M. A., and Coauthors, 2013a: *The atmospheric general circulation model ECHAM6 - Model description*, Berichte zur Erdsystemforschung / Max-Planck-Institut für Meteorologie, Vol. 135. Max-Planck-Institut für Meteorologie.

Giorgetta, M. A., and Coauthors, 2013b: Climate and carbon cycle changes from 1850 to 2100 in MPI-ESM simulations for the Coupled Model Intercomparison Project phase 5. *Journal of Advances in Modeling Earth Systems*, **5 (3)**, 572–597.

Goll, D. S., V. Brovkin, J. Liski, T. Raddatz, T. Thum, and K. E. Todd-Brown, 2015: Strong dependence of CO_2 emissions from anthropogenic land cover change on initial land cover and soil carbon parametrization. *Global Biogeochemical Cycles*, **29 (9)**, 1511–1523, doi:10.1002/2014GB004988.

González-Rouco, J. F., H. Beltrami, E. Zorita, and M. B. Stevens, 2009: Borehole climatology: a discussion based on contributions from climate modeling. *Clim. Past*, **5 (1)**, 97–127, doi:10.5194/cp-5-97-2009.

González-Rouco, J. F., and Coauthors, 2021: Increasing the depth of a Land Surface Model. Part I: Impacts on the soil thermal regime and energy storage. Submitted to Journal of Climate.

Gruber, S., 2012: Derivation and analysis of a high-resolution estimate of global permafrost zonation. *The Cryosphere; Katlenburg-Lindau*, **6 (1)**, 221–233, doi:10.5194/tc-6-221-2012.

Guillevic, P., R. D. Koster, M. J. Suarez, L. Bounoua, G. J. Collatz, S. O. Los, and S. P. Mahanama, 2002: Influence of the interannual variability of vegetation on the surface energy balance - A global sensitivity study. *Journal of Hydrometeorology*, **3 (6)**, 617–629, doi:10.1175/1525-7541(2002)003<0617:IOTIVO>2.0.CO;2.

Guo, Z., and Coauthors, 2006: GLACE: The Global Land-Atmosphere Coupling Experiment. Part II: Analysis. *J. Hydrometeor.*, **7 (4)**, 611–625, doi:10.1175/JHM511.1.

Hagemann, S., 2002: *An improved land surface parameter dataset for global and regional climate models*, Report: Max-Planck-Institut für Meteorologie, Vol. 336. Max-Planck-Institut für Meteorologie, dOI: 10.17617/2.2344576.

Hagemann, S., T. Blome, A. Ekici, and C. Beer, 2016: Soil-frost-enabled soil-moisture-precipitation feedback over northern high latitudes. *Earth Syst. Dynam.*, **7 (3)**, 611–625.

Hagemann, S., M. Botzet, L. Dümenil, and B. Machenhauer, 1999: Derivation of global GCM boundary conditions from 1 km land use satellite data.

Hagemann, S., A. Loew, and A. Andersson, 2013: Combined evaluation of MPI-ESM land surface water and energy fluxes. *Journal of Advances in Modeling Earth Systems*, **5 (2)**, 259–286, doi:10.1029/2012MS000173.

Hagemann, S., and T. Stacke, 2015: Impact of the soil hydrology scheme on simulated soil moisture memory. *Clim Dyn*, **44 (7-8)**, 1731–1750, doi:10.1007/s00382-014-2221-6.

Heimann, M., and M. Reichstein, 2008: Terrestrial ecosystem carbon dynamics and climate feedbacks. *Nature*, **451 (7176)**, nature06 591, doi:10.1038/nature06591.

Hermoso de Mendoza, I., H. Beltrami, A. H. MacDougall, and J.-C. Mareschal, 2020: Lower boundary conditions in land surface models - effects on the permafrost and the carbon pools: a case study with CLM4.5. *Geoscientific Model Development*, **13 (3)**, 1663–1683, doi:https://doi.org/10.5194/gmd-13-1663-2020.

Hillel, D., 1998: *Environmental Soil Physics*. Elsevier, New York.

Hong, S., V. Lakshmi, E. E. Small, F. Chen, M. Tewari, and K. W. Manning, 2009: Effects of vegetation and soil moisture on the simulated land surface processes from the coupled WRF/Noah model. *Journal of Geophysical Research*, **114 (D18)**, D18 118, doi:10.1029/2008JD011249.

Hugelius, G., and Coauthors, 2014: Estimated stocks of circumpolar permafrost carbon with quantified uncertainty ranges and identified data gaps. *Biogeosciences*, **11 (23)**, 6573–6593, doi:10.5194/bg-11-6573-2014.

Jackson, R. D., and S. A. Taylor, 1986: Thermal Conductivity and Diffusivity. *Klute, A. ed., SSSA Book Series, Methods of Soil Analysis: Part 1-Physical and Mineralogical Methods, 5.1:945-956*, Soil Science Society of America, American Society of Agronomy, doi:10.2136/sssabookser5.1.2ed.c39.

Jaeger, E. B., and S. I. Seneviratne, 2011: Impact of soil moisture-atmosphere coupling on European climate extremes and trends in a regional climate model. *Climate Dynamics*, **36 (9-10)**, 1919–1939, doi:10.1007/s00382-010-0780-8.

Johansen, O., 1977: Thermal Conductivity of Soils. Tech. Rep. CRREL-TL-637, COLD REGIONS RESEARCH AND ENGINEERING LAB HANOVER NH.

Jorgenson, M. T., C. H. Racine, J. C. Walters, and T. E. Osterkamp, 2001: Permafrost Degradation and Ecological Changes Associated with a WarmingClimate in Central Alaska. *Climatic Change*, **48 (4)**, 551–579, doi:10.1023/A:1005667424292.

Jungclaus, J. H., and Coauthors, 2013: Characteristics of the ocean simulations in MPIOM, the ocean component of the MPI Earth System Model. *Journal of Advances in Modeling Earth Systems*, **5**, 422–446, doi:10.1002/jame.20023.

Kleidon, A., and M. Heimann, 1998: A method of determining rooting depth from a terrestrial biosphere model and its impacts on the global water and carbon cycle. *Global Change Biology*, **4 (3)**, 275–286, doi:10.1046/j.1365-2486.1998.00152.x.

Koster, D., and Coauthors, 2006: GLACE: The Global Land-Atmosphere Coupling Experiment. 1. Overview. *J. Hydrometeor.*, **7 (4)**, 590–610, URL https://opensky.ucar.edu:/islandora/object/articles%3A10239/.

Koster, R. D., and M. J. Suarez, 2001: Soil moisture memory in climate models. *J. Hydrometeor.*, **2 (6)**, 558–570, doi:10.1175/1525-7541(2001)002<0558:SMMICM>2.0.CO;2.

Koster, R. D., and Coauthors, 2004: Regions of Strong Coupling Between Soil Moisture and Precipitation. *Science*, **305 (5687)**, 1138–1140, doi:10.1126/science.1100217.

Koven, C. D., W. J. Riley, and A. Stern, 2013: Analysis of Permafrost Thermal Dynamics and Response to Climate Change in the CMIP5 Earth System Models. *J. Climate*, **26 (6)**, 1877–1900, doi:10.1175/JCLI-D-12-00228.1.

Koven, C. D., B. Ringeval, P. Friedlingstein, P. Ciais, P. Cadule, D. Khvorostyanov, G. Krinner, and C. Tarnocai, 2011: Permafrost carbon-climate feedbacks accelerate global warming. *PNAS*, **108 (36)**, 14 769–14 774, doi:10.1073/pnas.1103910108.

Kumar, S., F. Zwiers, P. A. Dirmeyer, D. M. Lawrence, R. Shrestha, and A. T. Werner, 2016: Terrestrial contribution to the heterogeneity in hydrological changes under global warming. *Water Resour. Res.*, **52 (4)**, 3127–3142, doi:10.1002/2016WR018607.

Lawrence, D. M., and A. G. Slater, 2005: A projection of severe near-surface permafrost degradation during the 21st century. *Geophys. Res. Lett.*, **32 (24)**, L24 401, doi:10.1029/2005GL025080.

Lawrence, D. M., P. E. Thornton, K. W. Oleson, and G. B. Bonan, 2007: The partitioning of evapotranspiration into transpiration, soil evaporation, and canopy evaporation in a GCM: Impacts on land-atmosphere interaction. *Journal of Hydrometeorology*, **8 (4)**, 862–880, doi:10.1175/JHM596.1.

Levitus, S., and Coauthors, 2012: World ocean heat content and thermosteric sea level change (0-2000 m), 1955-2010. *Geophys. Res. Lett.*, **39 (10)**, L10 603, doi:10.1029/2012GL051106.

Loranty, M. M., and Coauthors, 2018: Reviews and syntheses: Changing ecosystem influences on soil thermal regimes in northern high-latitude permafrost regions. *Biogeosciences*, **15 (17)**, 5287–5313, doi:10.5194/bg-15-5287-2018.

Luo, L., and Coauthors, 2003: Effects of Frozen Soil on Soil Temperature, Spring Infiltration, and Runoff: Results from the PILPS 2(d) Experiment at Valdai, Russia. *J. Hydrometeor.*, **4 (2)**, 334–351, doi:10.1175/1525-7541(2003)4<334:EOFSOS>2.0.CO;2.

Lynch-Stieglitz, M., 1994: The Development and Validation of a Simple Snow Model for the GISS GCM. *J. Climate*, **7 (12)**, 1842–1855, doi:10.1175/1520-0442(1994)007<1842:TDAVOA>2.0.CO;2.

MacDougall, A. H., J. F. González-Rouco, M. B. Stevens, and H. Beltrami, 2008: Quantification of subsurface heat storage in a GCM simulation. *Geophys. Res. Lett.*, **35 (13)**, L13 702, doi:10.1029/2008GL034639.

MacDougall, A. H., K. Zickfeld, R. Knutti, and H. D. Matthews, 2015: Sensitivity of carbon budgets to permafrost carbon feedbacks and non-CO2 forcings. *Environmental Research Letters*, **10 (12)**, 125 003, doi:10.1088/1748-9326/10/12/125003.

Manabe, S., and R. J. Stouffer, 1980: Sensitivity of a global climate model to an increase of CO2 concentration in the atmosphere. *J. Geophys. Res.*, **85 (C10)**, 5529–5554, doi:10.1029/JC085iC10p05529.

Mareschal, J.-C., and H. Beltrami, 1992: Evidence for recent warming from perturbed geothermal gradients: examples from eastern canada. *Climate Dynamics*, **6 (3)**, 135–143, doi:10.1007/BF00193525.

Masson-Delmotte, V., and Coauthors, 2018: Global warming of 1.5°C An IPCC Special Report on the impacts of global warming of 1.5°C above pre-industrial levels and related global greenhouse gas emission pathways, in the context of strengthening the global response to the threat of climate change, sustainable development, and efforts to eradicate poverty. Tech. rep.

Masson-Delmotte, V., and Coauthors, 2019: Climate Change and Land An IPCC Special Report on climate change, desertification, land degradation, sustainable land management, food security, and greenhouse gas fluxes in terrestrial ecosystems Head of TSU (Operations) IT/Web Manager Senior Administrator. Tech. rep.

Mauritsen, T., and Coauthors, 2019: Developments in the MPI-M Earth System Model version 1.2 (MPI-ESM1.2) and Its Response to Increasing CO2. *Journal of Advances in Modeling Earth Systems*, **11 (4)**, 998–1038, doi:10.1029/2018MS001400.

Melo-Aguilar, C., J. F. González-Rouco, E. García-Bustamante, J. Navarro-Montesinos, and N. Steinert, 2018: Influence of radiative forcing factors on ground-air temperature coupling during the last millennium: implications for borehole climatology. *Climate of the Past*, **14 (11)**, 1583–1606, doi:10.5194/cp-14-1583-2018.

Menard, C. B., and Coauthors, 2021: Scientific and human errors in a snow model intercomparison. *Bulletin of the American Meteorological Society*, **102 (1)**, E61–E79, doi: 10.1175/BAMS-D-19-0329.1.

Mendoza, P. A., M. P. Clark, M. Barlage, B. Rajagopalan, L. Samaniego, G. Abramowitz, and H. Gupta, 2015: Are we unnecessarily constraining the agility of complex process-based models? *Water Resources Research*, **51 (1)**, 716–728, doi:10.1002/2014WR015820.

Nepstad, D. C., and Coauthors, 1994: The role of deep roots in the hydrological and carbon cycles of Amazonian forests and pastures. *Nature*, **372 (6507)**, 666–669, doi:10.1038/372666a0.

Nicolsky, D. J., V. E. Romanovsky, V. A. Alexeev, and D. M. Lawrence, 2007: Improved modeling of permafrost dynamics in a GCM land-surface scheme. *Geophys. Res. Lett.*, **34 (8)**, L08 501, doi:10.1029/2007GL029525.

Niu, G. Y., and Z. L. Yang, 2006: Effects of frozen soil on snowmelt runoff and soil water storage at a continental scale. *Journal of Hydrometeorology*, **7 (5)**, 937–952, doi:10.1175/JHM538.1.

Outcalt, S. I., F. E. Nelson, and K. M. Hinkel, 1990: The zero-curtain effect: Heat and mass transfer across an isothermal region in freezing soil. *Water Resources Research*, **26 (7)**, 1509–1516, doi:10.1029/WR026i007p01509.

Paquin, J.-P., and L. Sushama, 2015: On the Arctic near-surface permafrost and climate sensitivities to soil and snow model formulations in climate models. *Clim Dyn*, **44 (1)**, 203–228, doi:10.1007/s00382-014-2185-6.

Pollack, H. N., and S. Huang, 2000: Climate Reconstruction from Subsurface Temperatures. *Annual Review of Earth and Planetary Sciences*, **28 (1)**, 339–365, doi:10.1146/annurev.earth.28.1.339.

Reick, C. H., and Coauthors, 2021: JSBACH 3 - The land component of the MPI Earth System Model: documentation of version 3.2. Berichte zur Erdsystemforschung, 240. Tech. rep. doi:10.17617/2.3279802.

Rempel, A. R., and A. W. Rempel, 2016: Intrinsic Evaporative Cooling by Hygroscopic Earth Materials. *Geosciences*, **6 (3)**, 38, doi:10.3390/geosciences6030038.

Roeckner, E., and Coauthors, 2003: *The atmospheric general circulation model ECHAM 5. PART I: Model description*, Report / MPI für Meteorologie, Vol. 349.

Roesch, A., M. Wild, H. Gilgen, and A. Ohmura, 2001: A new snow cover fraction parametrization for the ECHAM4 GCM. *Climate Dynamics*, **17 (12)**, 933–946, doi:10.1007/s003820100153.

Romanovsky, V. E., S. L. Smith, and H. H. Christiansen, 2010: Permafrost thermal state in the polar northern hemisphere during the international polar year 2007-2009: A synthesis. *Permafrost and Periglacial Processes*, **21 (2)**, 106–116, doi:10.1002/ppp.689.

Sapriza-Azuri, G., P. Gamazo, S. Razavi, and H. S. Wheater, 2018: On the appropriate definition of soil profile configuration and initial conditions for land surface-hydrology models in cold regions. *Hydrology and Earth System Sciences*, **22 (6)**, 3295–3309, doi:https://doi.org/10.5194/hess-22-3295-2018.

Scholze, M., W. Knorr, and M. Heimann, 2003: Modelling terrestrial vegetation dynamics and carbon cycling for an abrupt climatic change event. *The Holocene*, **13 (3)**, 327–333, doi:10.1191/0959683603hl625rp.

Schuur, E. A. G., and Coauthors, 2008: Vulnerability of Permafrost Carbon to Climate Change: Implications for the Global Carbon Cycle. *BioScience*, **58 (8)**, 701–714, doi:10.1641/B580807.

Schuur, E. a. G., and Coauthors, 2015: Climate change and the permafrost carbon feedback. *Nature*, **520 (7546)**, 171, doi:10.1038/nature14338.

Seneviratne, S. I., T. Corti, E. L. Davin, M. Hirschi, E. B. Jaeger, I. Lehner, B. Orlowsky, and A. J. Teuling, 2010: Investigating soil moisthure-climate interactions in a changing climate: A review. *Earth-Science Reviews*, **99 (3)**, 125–161, doi:10.1016/j.earscirev.2010.02.004.

Seneviratne, S. I., and R. Stöckli, 2008: The Role of Land-Atmosphere Interactions for Climate Variability in Europe. *Climate Variability and Extremes during the Past 100 Years*, No. 33, Advances in Global Change Research, Springer Netherlands, 179–193, dOI: 10.1007/978-1-4020-6766-2_12.

Seneviratne, S. I., and Coauthors, 2006: Soil moisture memory in AGCM simulations: Analysis of global land-atmosphere coupling experiment (GLACE) data. *J. Hydrometeor.*, **7 (5)**, 1090–1112, doi:10.1175/JHM533.1.

Sentman, L. T., E. Shevliakova, R. J. Stouffer, and S. Malyshev, 2011: Time scales of terrestrial carbon response related to land-use application: Implications for initializing an earth system model. *Earth Interactions*, **15 (30)**, 1–16, doi:10.1175/2011EI401.1.

Slater, A. G., and D. M. Lawrence, 2013: Diagnosing Present and Future Permafrost from Climate Models. *J. Climate*, **26 (15)**, 5608–5623, doi:10.1175/JCLI-D-12-00341.1.

Slater, A. G., D. M. Lawrence, and C. D. Koven, 2017: Process-level model evaluation: a snow and heat transfer metric. *The Cryosphere*, **11 (2)**, 989–996, doi:10.5194/tc-11-989-2017.

Smerdon, J. E., H. N. Pollack, V. Cermak, J. W. Enz, M. Kresl, J. Safanda, and J. F. Wehmiller, 2004: Air-ground temperature coupling and subsurface propagation of annual temperature signals. *J. Geophys. Res.*, **109 (D21)**, D21 107, doi:10.1029/2004JD005056.

Smerdon, J. E., and M. Stieglitz, 2006: Simulating heat transport of harmonic temperature signals in the Earth's shallow subsurface: Lower-boundary sensitivities. *Geophys. Res. Lett.*, **33 (14)**, L14 402, doi:10.1029/2006GL026816.

Soong, J. L., C. L. Phillips, C. Ledna, C. D. Koven, and M. S. Torn, 2020: CMIP5 Models Predict Rapid and Deep Soil Warming Over the 21st Century. *Biogeosciences*, **125 (2)**, doi: 10.1029/2019JG005266.

Sorour, M. M., M. M. Saleh, and R. A. Mahmoud, 1990: Thermal conductivity and diffusivity of soil. **17 (2)**, 189–199, doi:10.1016/0735-1933(90)90053-M.

Stevens, B., and Coauthors, 2013: Atmospheric component of the MPI-M Earth System Model: ECHAM6. *J. Adv. Model. Earth Syst.*, **5 (2)**, 146–172, doi:10.1002/jame.20015.

Stevens, M. B., J. E. Smerdon, J. F. González-Rouco, M. Stieglitz, and H. Beltrami, 2007: Effects of bottom boundary placement on subsurface heat storage: Implications for climate model simulations. *Geophys. Res. Lett.*, **34 (2)**, L02 702, doi:10.1029/2006GL028546.

Stieglitz, M., S. J. Déry, V. E. Romanovsky, and T. E. Osterkamp, 2003: The role of snow cover in the warming of arctic permafrost. *Geophysical Research Letters*, **30 (13)**, doi:10.1029/2003GL017337.

Stieglitz, M., and J. E. Smerdon, 2007: Characterizing Land-Atmosphere Coupling and the Implications for Subsurface Thermodynamics. *J. Climate*, **20 (1)**, 21–37, doi:10.1175/JCLI3982.1.

Stocker, T., and Coauthors, 2013: *Climate Change 2013: The Physical Science Basis. Contribution of Working Group I to the Fifth Assessment Report of the Intergovernmental Panel on Climate Change*. Cambridge University Press, Cambridge, United Kingdom and New York, NY, USA, doi:10.1017/CBO9781107415324.

Sun, S., and X. Zhang, 2004: Effect of the lower boundary position of the Fourier equation on the soil energy balance. *Adv. Atmos. Sci.*, **21 (6)**, 868–878, doi:10.1007/BF02915589.

Swenson, S. C., D. M. Lawrence, and H. Lee, 2012: Improved simulation of the terrestrial hydrological cycle in permafrost regions by the Community Land Model. *Journal of Advances in Modeling Earth Systems*, **4 (3)**, doi:10.1029/2012MS000165.

Tarnocai, C., J. G. Canadell, E. a. G. Schuur, P. Kuhry, G. Mazhitova, and S. Zimov, 2009: Soil organic carbon pools in the northern circumpolar permafrost region. *Global Biogeochem. Cycles*, **23 (2)**, GB2023, doi:10.1029/2008GB003327.

Taylor, K. E., R. J. Stouffer, and G. A. Meehl, 2012: An Overview of CMIP5 and the Experiment Design. *Bull. Amer. Meteor. Soc.*, **93 (4)**, 485–498, doi:10.1175/BAMS-D-11-00094.1.

Turcotte, D., and G. Schubert, 2014: *Geodynamics*. Cambridge University Press.

van Vuuren, D. P., and Coauthors, 2011: The representative concentration pathways: An overview. *Climatic Change*, **109 (1)**, 5–31, doi:10.1007/s10584-011-0148-z.

Voigt, C., and Coauthors, 2017: Increased nitrous oxide emissions from Arctic peatlands after permafrost thaw. *Proceedings of the National Academy of Sciences of the United States of America*, **114 (24)**, 6238–6243, doi:10.1073/pnas.1702902114.

von Schuckmann, K., and Coauthors, 2020: Heat stored in the Earth system: Where does the energy go? The GCOS Earth heat inventory team. *Earth System Science Data Discussions*, 1–45, doi:https://doi.org/10.5194/essd-2019-255, publisher: Copernicus GmbH.

Wang, F., F. Cheruy, and J. L. Dufresne, 2016: The improvement of soil thermodynamics and its effects on land surface meteorology in the IPSL climate model. *Geoscientific Model Development*, **9 (1)**, 363–381, doi:10.5194/gmd-9-363-2016.

Warrilow, D. A., 1986: *Modelling of Land Surface Processes and Their Influence on European Climate*. Met 0 20 (Dynamical Climatology Branch), Meteorological Office.

Woo, M.-k., 2012: *Permafrost Hydrology*. Springer-Verlag, Berlin Heidelberg.

Zhang, T., R. G. Barry, K. Knowles, J. A. Heginbottom, and J. Brown, 2008: Statistics and characteristics of permafrost and ground-ice distribution in the Northern Hemisphere. *Polar Geography*, **31 (1-2)**, 47–68, doi:10.1080/10889370802175895.

Zhang, T., and Coauthors, 2005: Spatial and temporal variability in active layer thickness over the Russian Arctic drainage basin. *J. Geophys. Res.*, **110 (D16)**, D16 101, doi: 10.1029/2004JD005642.

LIST OF TABLES

TABLE 1. Experiment names and corresponding model configuration setups for bottom boundary condition depth (BBCP), soil parameter datasets (SPD), hydro-thermodynamic soil coupling (HTC; off=standard version JSBACH-REF, on=JSBACH-HTC version with improved soil physics), supercooled water (SCW), dynamic calculation of soil thermal properties (DCC), water phase changes (LHE), and improved snow model (SNOW). All experiments were run for a piControl spin-up (years 0–500) following González-Rouco et al. (2021). The top eight experiments were run for the historical (1850–2005) and RCP2.6, RCP4.5 and RCP8.5 (2006–2100) conditions, respectively. Only 30 years of the historical period (1850–1879) were simulated for the bottom four experiments in order to investigate the sensitivity to the individual contribution of the four JSBACH-HTC physical mechanisms: LHE, DCC, SCW and SNOW. Note that the naming of these experiments addresses the impact of changing only one parameter at a time, which makes an assessment of the single processes possible (also see Section 3.c).

Name	BBCP	SPD	HTC	SCW	DCC	LHE	SNOW
REF_SPD1s	shallow	SPD1	off	yes	no	no	no
HTC_SPD1s	shallow	SPD1	on	no	yes	yes	yes
REF_SPD2s	shallow	SPD2	off	yes	no	no	no
HTC_SPD2s	shallow	SPD2	on	no	yes	yes	yes
REF_SPD1d	deep	SPD1	off	yes	no	no	no
HTC_SPD1d	deep	SPD1	on	no	yes	yes	yes
REF_SPD2d	deep	SPD2	off	yes	no	no	no
HTC_SPD2d	deep	SPD2	on	no	yes	yes	yes
HTC_LHE	deep	SPD1	on	no	yes	no	yes
HTC_DCC	deep	SPD1	on	no	no	yes	yes
HTC_SCW	deep	SPD1	on	yes	no	yes	yes
HTC_SNOW	deep	SPD1	on	yes	no	no	yes

LIST OF FIGURES

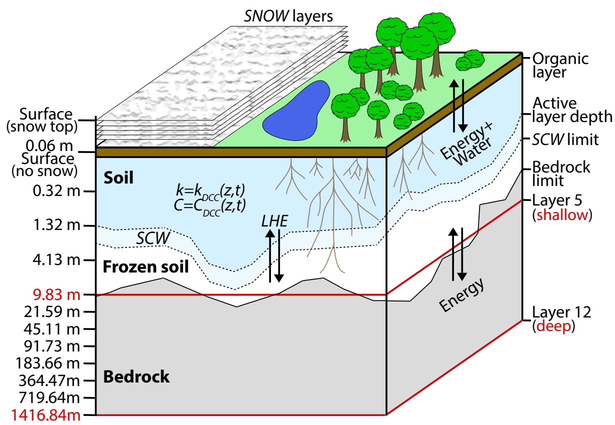

FIG. 1. Simplified vertical scheme of the JSBACH Land Surface Model component in the northern high latitudes. The shallow (5-layer) and deep (12-layer) BBCP-depth configurations are marked in red. Soil depth (bedrock limit) varies in every model grid point as prescribed by the respective soil parameter dataset (SPD). Soil moisture is present above the bedrock only. The representation of snow (SNOW), dynamic soil thermal properties (DCC, with k=thermal conductivity and C=heat capacity), Latent heat transfer (LHE) and supercooled water (SCW) are regulated by the given model configurations of hydro-thermodynamic soil coupling. See Figure 1 in González-Rouco et al. (2021) for a comparison of the differences in model features considered herein.

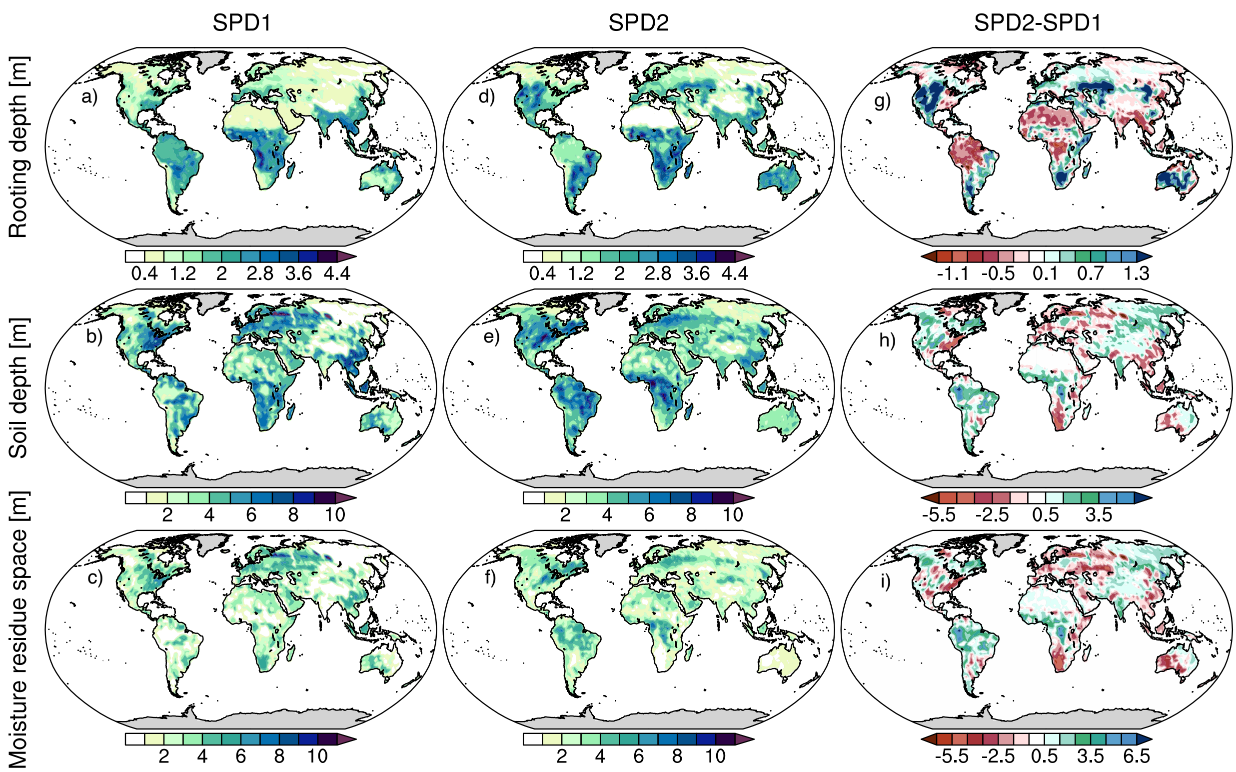

FIG. 2. Soil parameter datasets SPD1 (a–c) and SPD2 (d–f) and their differences (g–i) for rooting depth [m], soil (bedrock) depth [m], and soil moisture residue space [m] that are related to the spatial distribution and temporal availability of moisture in the soil. Moisture residue space is defined by the vertical area between the plant rooting depth and the soil depth (bedrock limit) and thus is described by the difference between the upper two rows of figures.

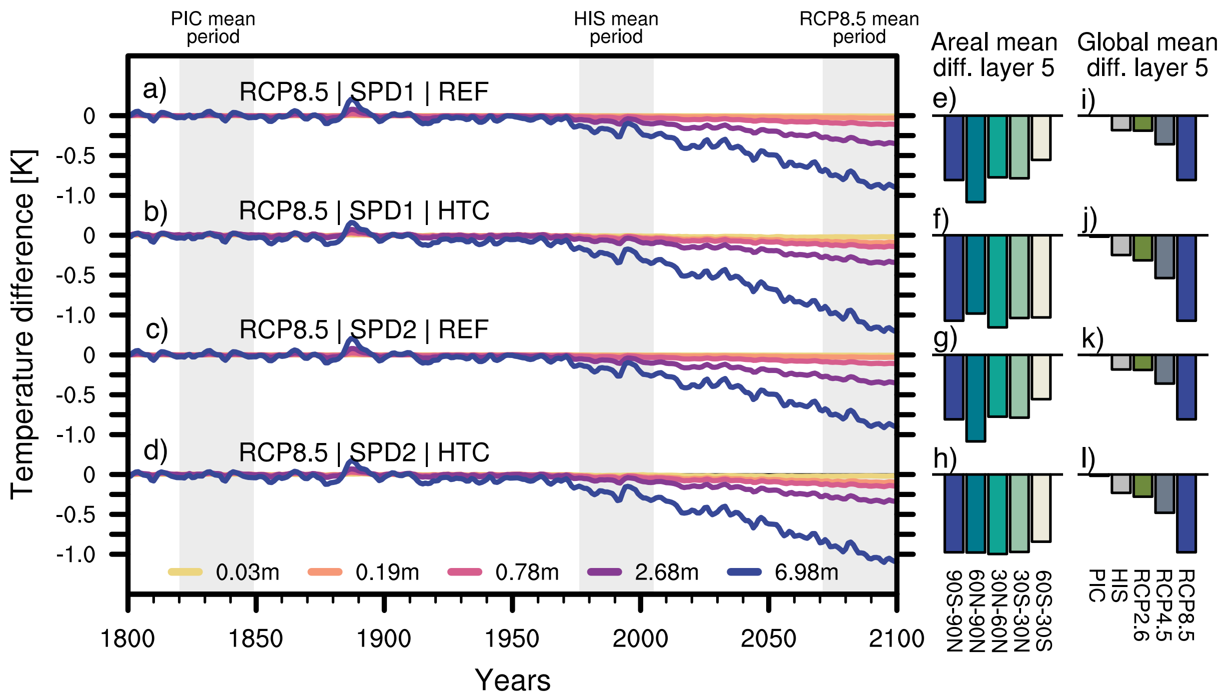

FIG. 3. Soil temperature differences [K] (a–d) at the first 5 model layers (see Fig. 1) between the deep and the shallow model configurations for different combinations of JSBACH-REF and JSBACH-HTC with two different soil parameter datasets (SPD1 and SPD2; see Table 1 for experiment description). Global means for 300 years are shown continuously for the piControl+historical+RCP8.5 scenario simulations. Global and latitudinal band means of the last 30-years (2071–2100) of the scenario period (e–h) and different forcing scenarios (i–l). The bar plots are based on the respective last 30 years of the PIC (1821–1850), HIS (1976–2005) and RCP scenario (2071–2100) periods, marked by the gray shaded areas in a)–d).

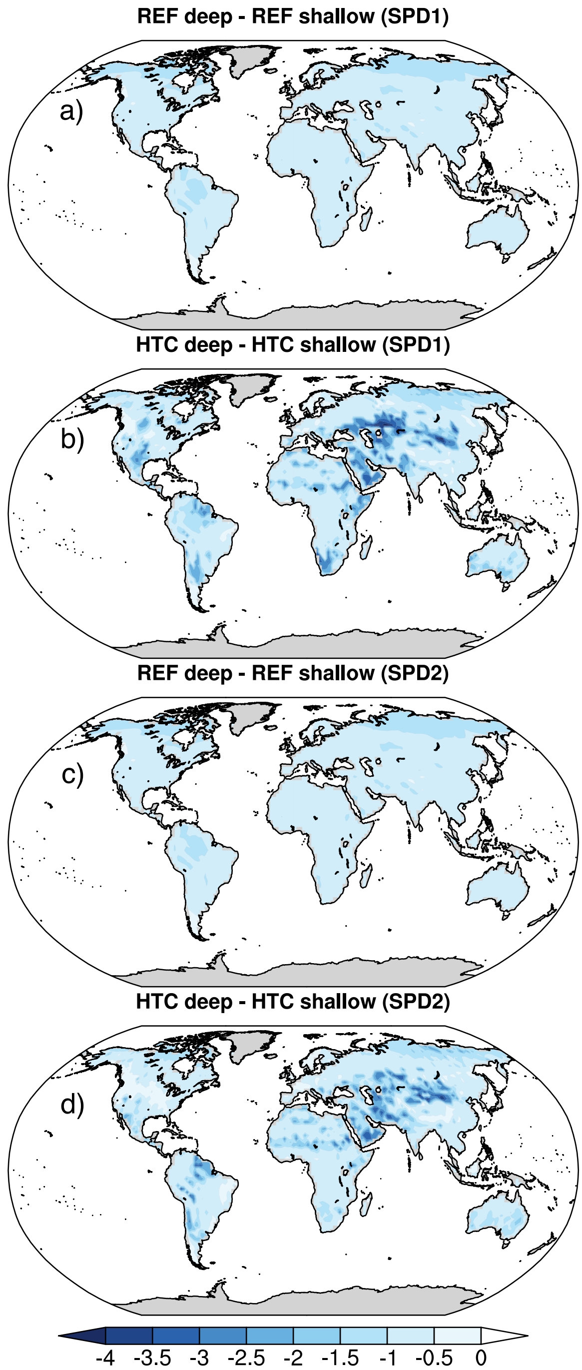

FIG. 4. Soil temperature differences [K] at model layer 5 between the deep and the shallow model configurations for different combinations of hydro-thermodynamic soil coupling (JSBACH-REF: a,b; and JSBACH-HTC: b,d) and soil parameter datasets (SPD1: a,b; and SPD2: c,d). Differences are significant (Student's t-test, $p<0.05$) at all grid points.

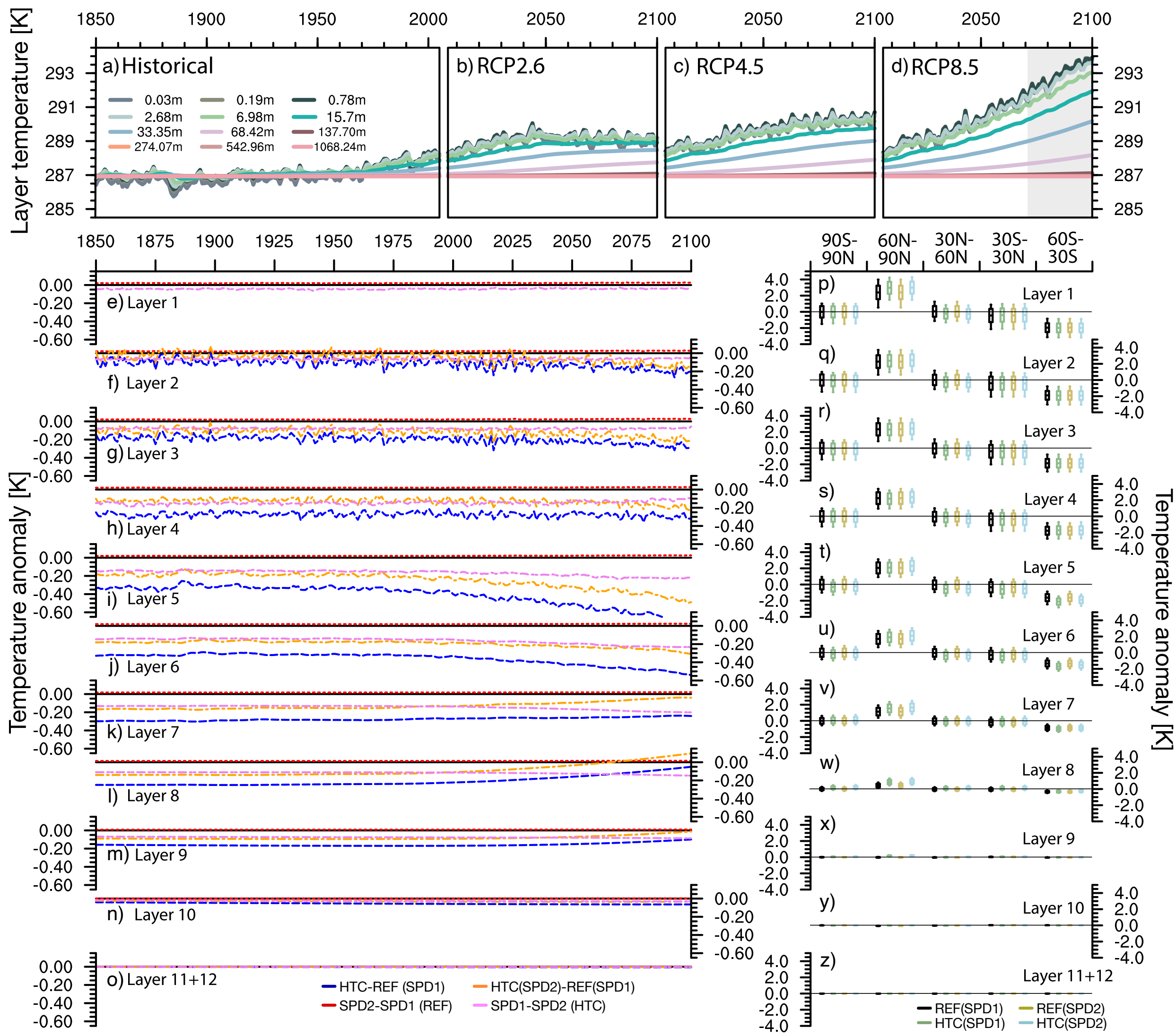

FIG. 5. Global mean soil temperatures [K] at layers 1–12 of the deep model (a–d) in the simulation with JSBACH-REF and SPD1 (REF_SPD1d) for the historical period (1850–2005) and RCP2.6, RCP4.5 and RCP8.5 scenarios (2006–2100; Table 1). Soil temperature differences for each layer (e–o) as anomalies to the first 30-year average (1850–1879) of the historical period for every layer of the deep model configuration with JSBACH-REF and SPD1. Temperature differences are presented as comparisons between different configurations of HTC and SPD (see legend for colors). Note that for visibility, the pink line is SPD1-SPD2, since the reverse would produce positive values with JSBACH-HTC. Temperature anomalies for each layer (p–z) of the last 30-year average (2071–2100; see gray shaded area in top panel) of the RCP8.5 scenario period to the first 30-year mean (1850–1879) of the historical period for the global mean and latitudinal band averages in simulations with different configurations of HTC and SPD in every layer of the 12-layer deep model configuration. The centers of the boxes indicate the mean value, box bounds are the standard deviation, and whiskers refer to the extreme values of the last 30-year period of anomalies of the time series in the left column.

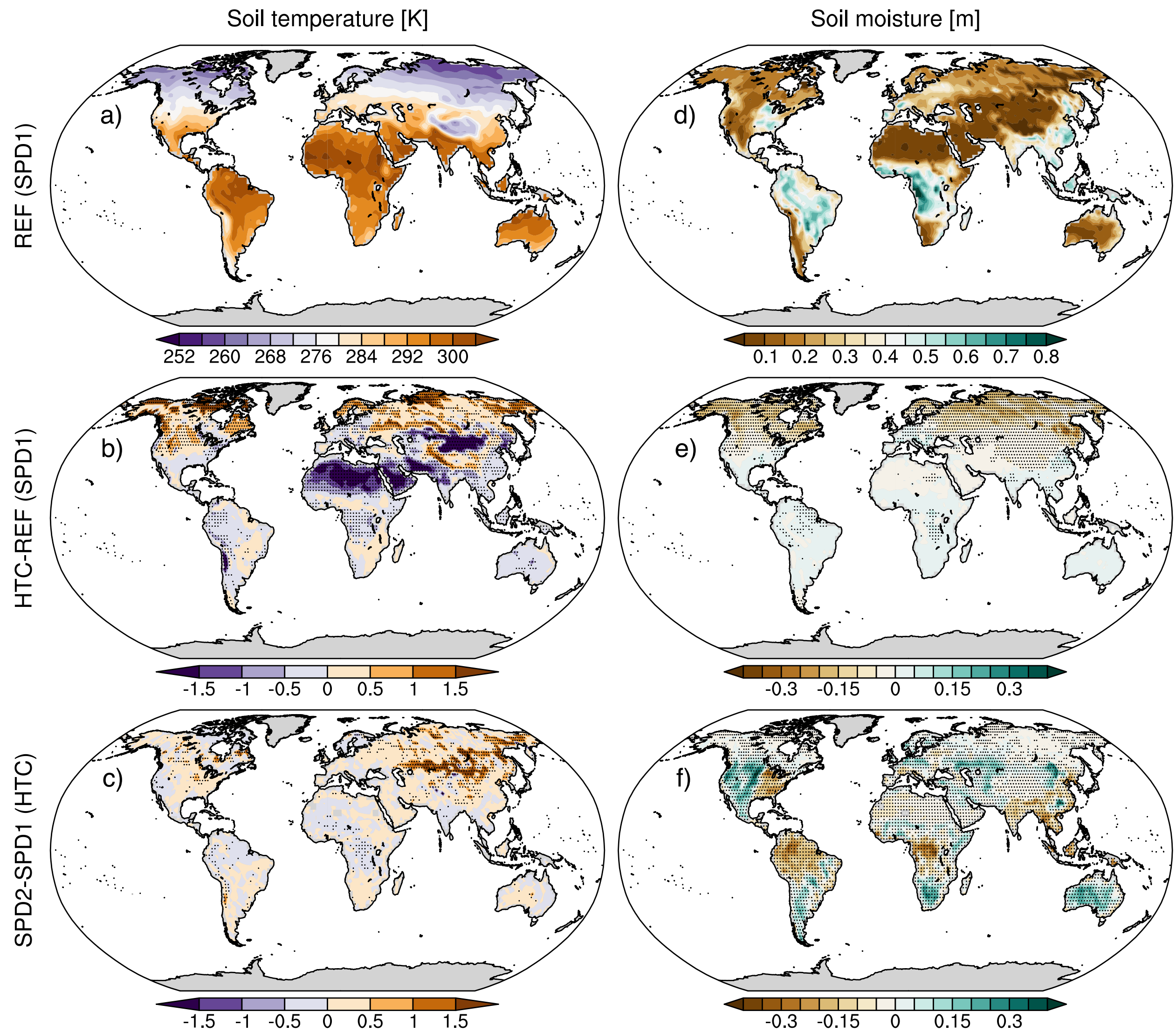

FIG. 6. Climatological mean (1850–1879) of soil column (average of top 5 layers) temperature (a–c) and vertically integrated root zone soil moisture (d–f) of JSBACH-REF (a,d) and the differences between JSBACH-HTC and JSBACH-REF (b,d), as well as differences between the soil parameter datasets SPD1 and SPD2 (c,f) for soil temperature [K] and moisture [m], respectively. Stippling indicates significant differences of a Student's t-test ($p<0.05$).

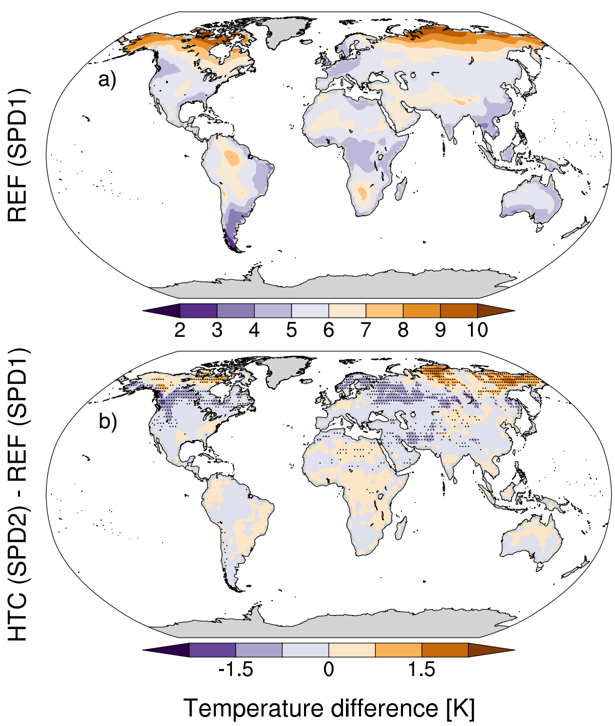

FIG. 7. Soil column (average of top 5 layers) temperature anomaly [K] of RCP8.5 (2071–2100) with respect to pre-industrial conditions 1850–1879 of JSBACH-REF with SPD1 (a). Differences with respect to a) of the combined effect of hydro-thermodynamic soil coupling and soil parameter datasets on soil temperature anomalies [K] between the periods 2071–2100 and 1850–1879 (b). See Table 1 for experiment configurations. Stippling indicates significant differences of a Student's t-test (p<0.05).

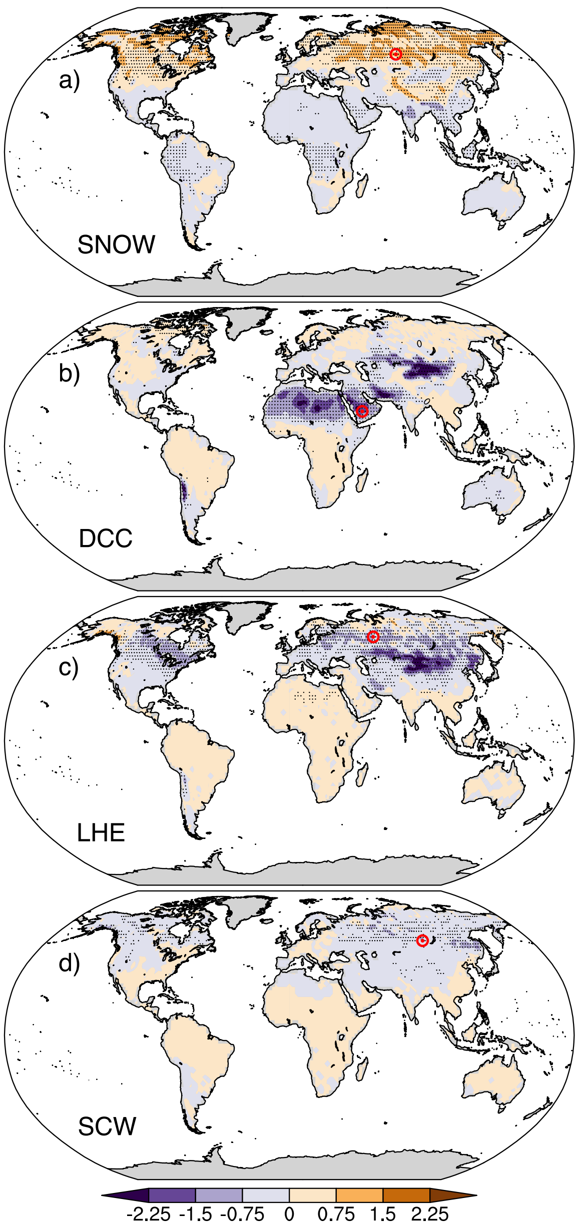

FIG. 8. Soil temperature [K] response (vertical average of layers 1–5) of the four contributing physical mechanisms of the hydro-thermodynamic coupled soil HTC: 5-layer snow model (a; SNOW = HTC_SNOW - REF_SPD1d), dynamic moisture-dependent calculation of soil thermal conductivity and heat capacity (b; DCC = HTC_SPD1d - HTC_DCC), soil water phase changes (c; LHE = HTC_SPD1d - HTC_LHE), and the implementation of supercooled water (d; SCW = HTC_SCW - HTC_DCC). Also see Table 1 for experiment configurations. Red dots indicate locations that are referred to in the following figures (Figs. 9,10,11 and 12) for each of the four HTC-cases.Stippling indicates significant differences of a Student's t-test (p<0.05).

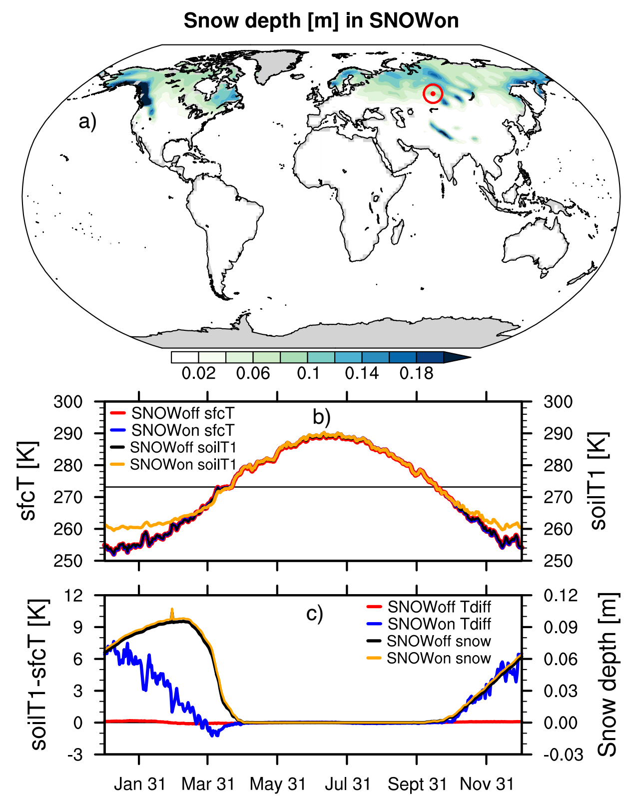

FIG. 9. Climatological (1850–1879) winter (DJF) mean of snow depth [m] (a). Surface temperature [K] (sfcT) and layer 1 soil temperature [K] (soilT1; b) and their differences (c) in the snow model configurations SNOWoff and SNOWon for annual daily mean values over the period 1850–1879 at the indicated location (red in a); and indicated in Figure 8a). SNOWon and SNOWoff refer to the HTC_SNOW and REF_SPD1d simulations, respectively (see Tab. 1 for an overview of the experiment configurations).

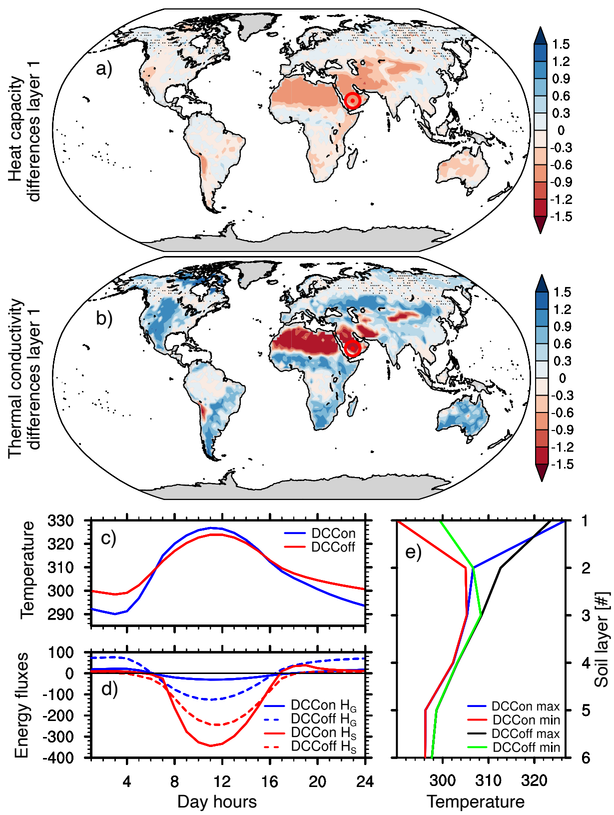

FIG. 10. Layer 1 (0.03 m mid-layer depth) heat capacity [10^6 $\mathrm{Jm^{-3}K^{-1}}$] difference (a) and thermal conductivity [$\mathrm{Jm^{-1}s^{-1}}$] difference (b) between DCCon and DCCoff. Stippling indicates significant differences of a Student's t-test (p<0.05). Layer 1 soil temperature [K] (c) and soil energy fluxes [Wm^{-2}] (d) as sensible heat flux at the surface (H_S) and ground heat flux between the 1st and 2nd soil layers (H_G) shown as hourly means of August 1859 at the indicated location (red dot in in a) and b); and indicated in Figure 8b) in DCCon and DCCoff. Soil temperature profile (e) of the mean daily extrema of August 1859 at the indicated location (black dot in maps) in DCCon and DCCoff. DCCon and DCCoff refer to the REF_SPD1d and HTC_DCC simulations, respectively (see Tab. 1 for an overview of the experiment configurations).

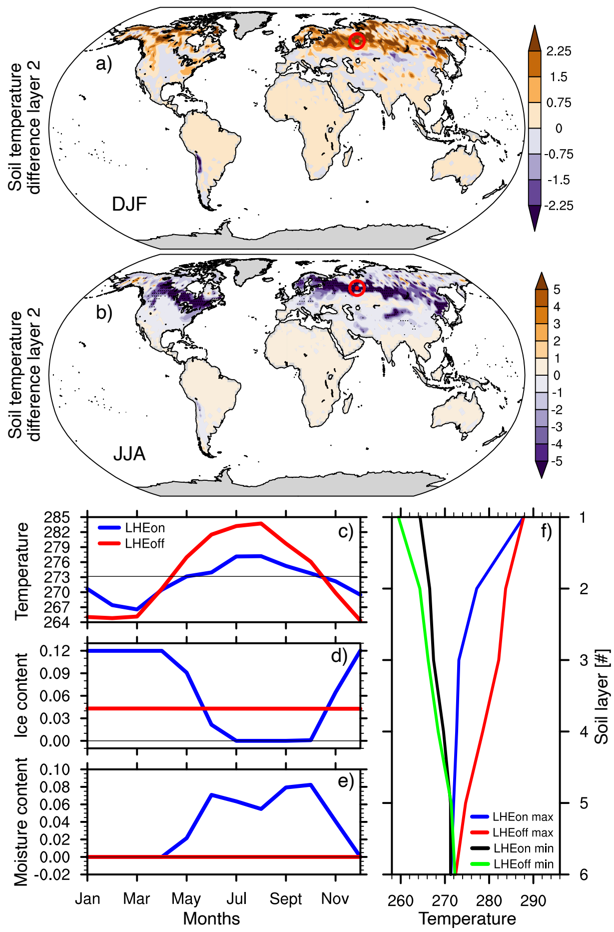

FIG. 11. Spatial distribution of soil temperature differences [K] at layer 2 (0.19 m mid-layer depth) for winter (DJF; a) and summer (JJA; b). Stippling indicates significant differences of a Student's t-test ($p<0.05$). Layer 2 soil temperature [K] (c), ice content [m] (d) and moisture [m] (e) of LHEon and LHEoff as monthly means of the year 1861, and soil temperature profile (f) of LHEon and LHEoff of 1861 extrema at each layer at the location (red dot in a) and b); and indicated in Figure 8c). LHEon and LHEoff refer to the HTC_SPD1d and HTC_LHE simulations, respectively (see Tab. 1 for an overview of the experiment configurations). Note that both LHEon and LHEoff are HTC-simulations, which is why, ice content in LHEoff is not zero.

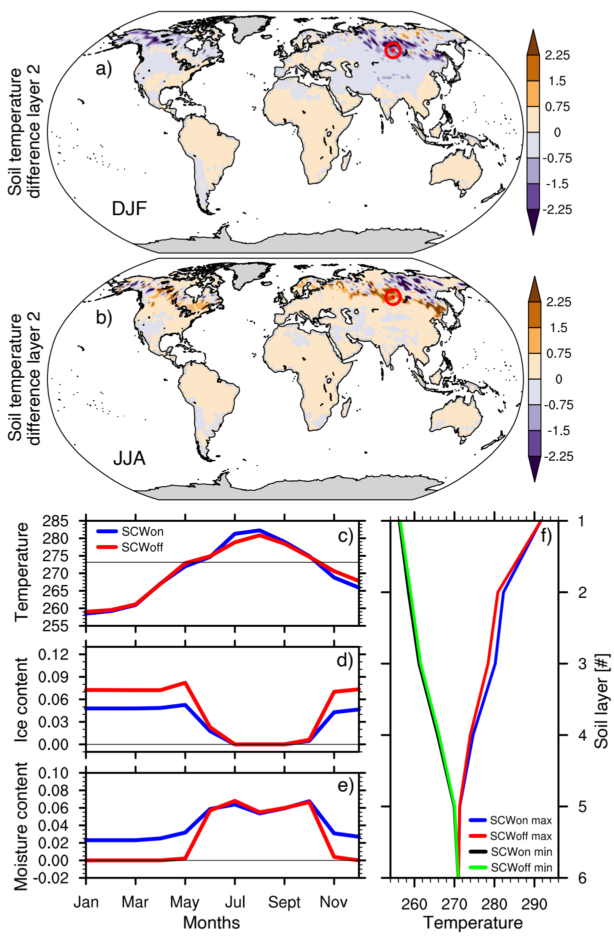

FIG. 12. Spatial distribution of soil temperature differences [K] at layer 2 (0.19 m mid-layer depth) for winter (DJF; a) and summer (JJA; b). Stippling indicates significant differences of a Student's t-test ($p<0.05$). Layer 2 soil temperature [K] (c), ice content [m] (d) and moisture [m] (e) of SCWon and SCWoff as monthly means of the year 1861, and soil temperature profile (f) of SCWon and SCWoff of 1861 extrema at each layer at the location (red dot in a) and b); and indicated in Figure 8d). SCWon and SCWoff refer to the HTC_SCW and HTC_DCC simulations, respectively (see Tab. 1 for an overview of the experiment configurations).

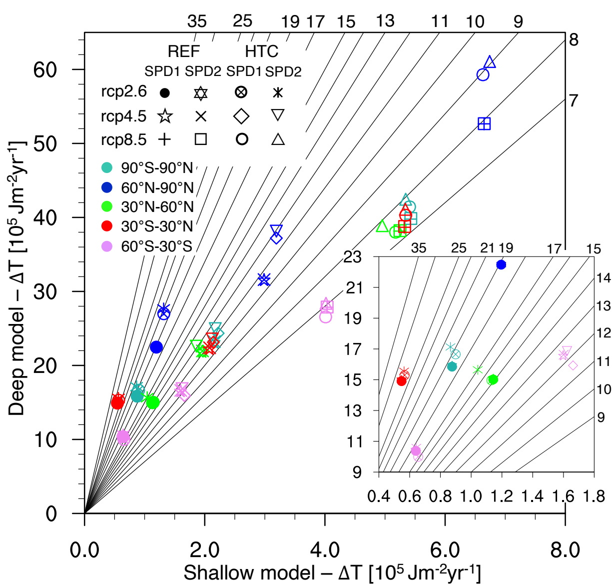

FIG. 13. Regional annual mean heat content change ΔQ [$10^5 \mathrm{Jm}^{-2}\mathrm{yr}^{-1}$] for the shallow (x-axis) vs the deep (y-axis) model for different soil hydrological conditions of HTC and SPD in the RCP2.6, RCP4.5 and RCP8.5 scenario projections. Black lines and the corresponding number at the right and top axis correspond to multipliers between the shallow and deep configurations. The inset provides a zoom into the lower part of the scale.

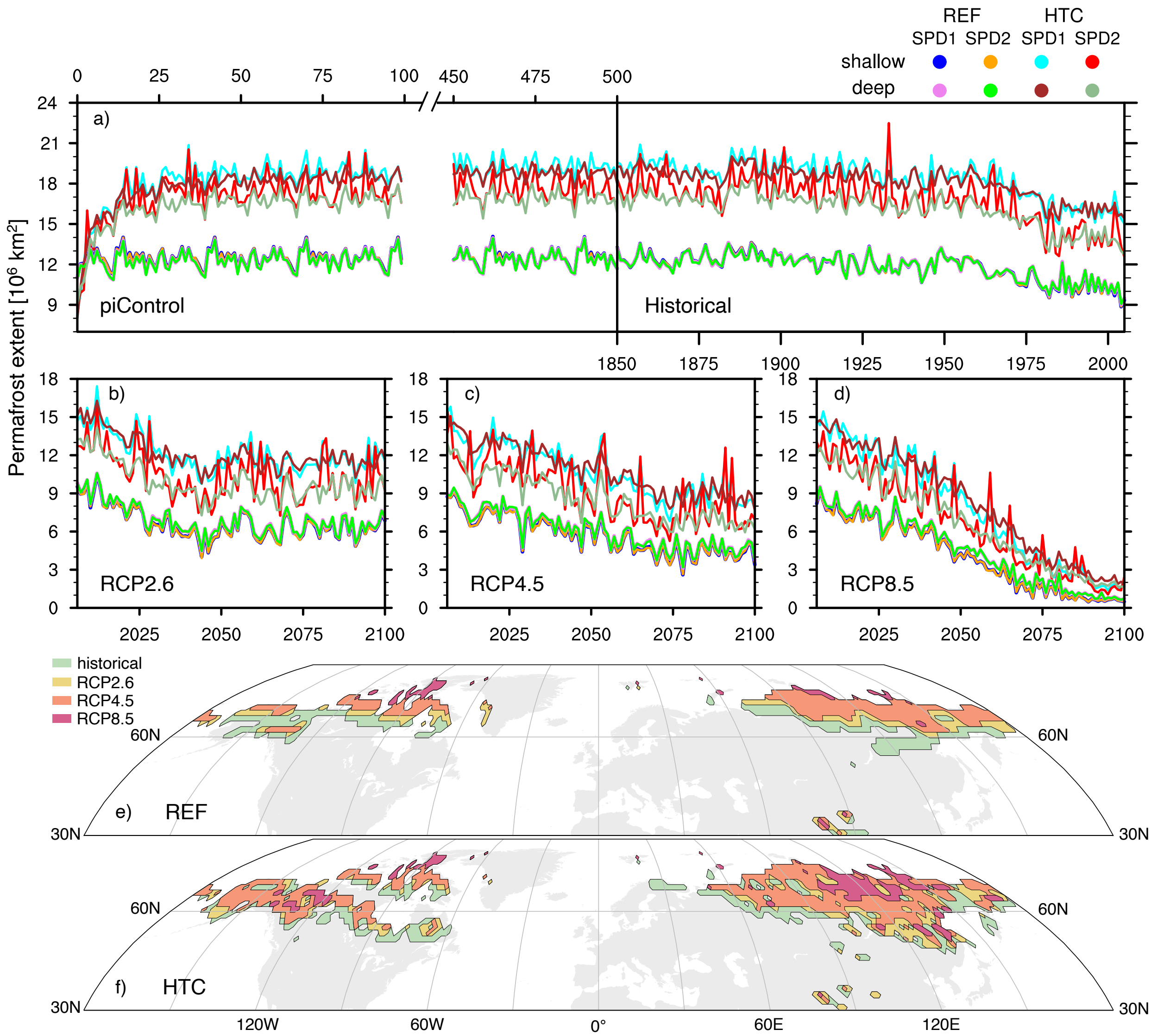

1339 FIG. 14. Permafrost extent (10^6 km^2; 45–90N) in different soil hydrological HTC and SPD conditions (colors) from PIC and HIS (a) to RCP2.6 (b), RCP4.5 (c) and RCP8.5 (d) forcing conditions. Spatial permafrost in JSBACH-REF (e) and JSBACH-HTC (f) in the deep model with SPD1 for decadal means of HIS (1980–1990, green), RCP2.6 (2090–2100, yellow), RCP4.5 (2090–2100, orange) and RCP8.5 (2090–2100, red).

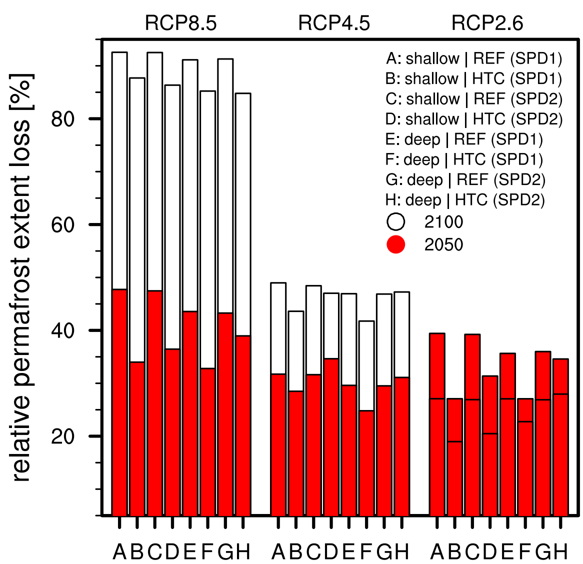

FIG. 15. Relative permafrost extent loss [%] for different configurations of hydro-thermodynamic soil coupling (HTC) and soil parameter datasets (SPD) in the shallow (5-layer) and the deep (12-layer) model for the years 2050 (red bars), and 2100 (white bars) in the RCP2.6, RCP4.5 and RCP8.5 forcing scenarios. For RCP2.6, the relative permafrost extent loss in 2100 is less than in 2050, which causes the overlaying red bars.